Modeling Seismic Hazard and Landslide Occurrence Probabilities~~Potentials~~ in Northwestern Yunnan, China: Exploring Complex Fault Systems with multi-segment rupturing in a Block Rotational Tectonic Zone

Jia Cheng[1*], Chong Xu[2], Xiwei Xu[1], Shimin Zhang[2], Pengyu Zhu[2]

1. School of Earth Sciences and Resources, China University of Geosciences (Beijing),

   Beijing, 100083, China

2. National Institute of Natural Hazards, Ministry of Emergency Management of China,

   Beijing, 100085, China

*Corresponding author:

Jia Cheng (jiacheng@cugb.edu.cn, jiacheng@gmail.com)

Address: China University of Geosciences (Beijing), No. 29, Xueyuan Road, Haidian,

Beijing, 100083, China

Phone: +86-10-13466515670

Fax: +86-10-82322264

Abstract

The Northwestern Yunnan Region ~~(NWYR)~~, located on the southeastern edge of the Tibetan Plateau, is characterized by a combination of ~~low crustal flow~~ductile flow of the lower crust with low shear-wave velocity ~~and gravitational collapse, giving rise to a complex network of active faults. This presents significant seismic hazards, particularly due to the potential for multi-segment ruptures and resulting landslides~~, as demonstrated by the historical 1515 *M*7.8 Yongshen Earthquake~~. This article presents

25 ed a newnovel seismic hazard modeling study for the Northwestern Yunnan

26 RegionNWYR, , incorporating recent findings on fault geometry and slip rates

27 alongintegrating fault slip parameters with historical seismicity rates toand assessing

28 multi-segment rupturing risks. Among the four potential multi-segment rupture

29 combination models examined, Model 1, characterized by multi-segment rupture

30 combinations on singlesingle faults, particularly fracturing the Zhongdian fault, is

31 proposed asemerges as the most suitable for the Northwestern Yunnan RegionNWYR,

32 given that the non-mainshock slip (NMS) ratios on fault segments are all below the

33 30%~40% threshold, as supported by the alignment agreement of modeled seismicity

34 rates with fault slip rates. Our analysis demonstrates demonstratesshows d that the Peak

35 Ground-motion Acceleration (peak ground motion acceleration (PGA)) values for a

36 mean return period, calculated with of a 475 -years, which is calculated with the

37 developed probabilistic seismic hazard model, return period from modeled seismicity

38 rates, exhibitedhas a strong correlation with the spatial distribution of the faults. Ofault

39 distribution, on average, these values arely higher than the the PGAose given provided

40 by the China Seismic Ground Motion Parameters Zonation Map. Furthermore, we

41 utilized PGA values with the Bayesian Probability Method and a Machine Learning

42 Model to predict landslide occurrence probabilities, as a function of based on our PGA

43 distribution mapwe conducted simulations to forecast landslide occurrence

44 probabilities across our peak ground motion acceleration distribution map. Our

45 findings underscored that the observed combinations of multi-segment ruptures and

46 their associated behaviors were in alignment with the small block rotation triggered by

the gravitational collapse of the Tibetan Plateau. This result highlightsed the intricate interplay between multi-segment rupturing hazards and regional geological dynamics, ,while also providing valuable guidance for disaster preparedness efforts.

Key Words:

Northwestern Yunnan Region; multi-segment rupture; probability seismic hazard analysis; landslide risk probabilities

1. Introduction

The collision of the Eurasian Platea and the Indian plate makes the Tibetan Plateau, the world's highest, with altitude of 4000+ m averagely. The eastern extrusion of the crust in the Tibetan Plateau, associated with the wedged Eastern Himalayan syntaxis, initiateds a clockwise rotation of crustal deformation in the southeastern margin of the Tibetan Plateau (Figure 1) (Zhang et al., 2004; Gan et al., 2007; Wang and Shen, 2020). The Northwestern Yunnan Region (NWYR), in the west part of the southeastern margin of the Tibetan Plateau, borders the Tibetan Plateau, with the Lijiang-Xiaojiang fault serving as a boundary fault. This fault that separates the Tibetan Plateau, boasting an average altitude of over 3000 meters, from the Yunnan Region, which maintains an average altitude of over 2000 meters (Yu et al., 2022; Zhang et al., 2022) (see Figure 1). Unlike the thrust faults alongin the plateau boundary, such as the Longmenshan fault

69 ruptured by the 2008 M_W7.9 Wenchuan earthquake, the Holocene slip type of the

70 Lijiang-Xiaojinhe fault is sinistral, with a strike-slip rate of ~~approximately~~ ~ 3 mm/yr,

71 ~~as determined by~~from geological (Xu et al., 2003; Shen et al., 2005; Ding et al., 2018;

72 Gao et al., 2019) and geodetic data (Gan et al., 2007; Cheng et al., 2012).

73 The peculiar slip behavior of the Lijiang-Xiaojinhe fault has garnered considerable

74 attention in studies pertaining to crustal structure, fault activities, and earthquake

75 hazards (Xu et al., 2003; Cheng et al., 2012; Zhao et al., 2013; Bao et al., 2015; Zhang

76 et al., 2020; Huang et al., 2022; Zhang et al., 2022; Dai et al., 2023). Zhang et al. (2020)

77 employed ,a shear-wave velocity model ~~was employed~~ to reveal that three faults---the

78 Longmenshan fault, the Lijiang-Xiaojinhe fault, and the Chenghai fault—-

79 outline~~delineate~~ a low-velocity belt in the lower crust. This investigation

80 un~~covered~~veiled the presence of low-crustal flow beneath the ~~Northwestern Yunnan~~

81 ~~Region~~ (NWYR~~)~~. Similarly, Zhang et al. (2022) utilized magnetotelluric (MT)

82 observations in the southern vicinity of the Lijiang-Xiaojinhe fault, corroborating these

83 findings and ~~emphasizing~~highlighting the NWYR as a ~~pathway~~conduit for ductile low-

84 crustal flow in 10 km depth. Analogously, a GPS study by Cheng et al. (2012) yielded

85 comparable results.

86 Upon ~~eliminatin~~removing~~g~~ the rigid rotation component from the regional GPS

87 velocity field, they demonstrated a clockwise rotation ~~propelled~~ driven by ductile

88 crustal flow, particularly accelerated within the NWYR. They posited that this

89 acceleration in clockwise rotation might also be intensified by the tensional drag

90 originating from the Burma Plate.

The intricate network of crustal deformation encompassing the ~~Northwestern Yunnan Region (~~NWYR~~)~~ introduces complexity to the slip behavior of faults~~ and the focal mechanisms of recent earthquakes~~. Within this area, three distinct fault slip behaviors are observed: the NE-trending Lijiang-Xiaojinhe fault displays left-lateral strike-slip, NW-trending faults exhibit right-lateral strike-slip, and North-South trending faults demonstrate normal slip (see Figure 2). The presence of faults with diverse rupture behaviors ~~contribute~~contributes~~s~~ to the complexity of earthquake hazards. Historically, these faults have been associated with significant seismic events and numerous casualties. Notably, three earthquakes with M7+ ~~have~~ occurred in the NWYR: the Yongsheng earthquake of 1515 ($\sim M$7.5) on the Chenghai fault, the Midu earthquake of 1652 ($\sim M$7) on the Red River fault, and the Dali earthquake of 1925 ($\sim M$7) on the Diancangshan East fault. Additionally, the 1990 Lijiang earthquake (M_S7.0/M_W6.6) occurred on the Yulong East fault, exhibiting dominant normal slip behavior. Historical and paleo-earthquake studies suggest that nearly all of these faults have the potential to generate catastrophic earthquakes (e.g., Ding et al., 2018; Ren et al., 2007; Chang et al., 2014), and induced numerous landslides (Institute of Geology-State Seismological Bureau, and Yunnan Seismological Bureau, 1990; Huang et al. 2021).

Fieldwork studies and focal mechanisms of recent earthquakes underscore the complexity of fault slip behaviors in this tectonic environment (Figure 2). Both historical and instrumental earthquakes have affected nearly all faults in the region, emphasizing the seismic risks in NWYR. For instance, the 2013 Deqin earthquake swarm, reaching a maximum magnitude of M_S5.9/M_W5.7 on August 31 (Wu et al.,

2015), and the 2021 Yangbi earthquake swarm, reaching a maximum magnitude of $M_S5.9/M_W6.1$ on May 21 (Zhou et al., 2022), are noteworthy seismic events (Figure 2). The 2013 $M_W5.7$ Deqin earthquake swarm, characterized by tensional stress, occurred at the intersection of the Zhongdian fault and the southern part of the Jinshajiang fault, illustrating the susceptibility of the regional stress field to disturbance. Conversely, the 2021 $M_W6.1$ Yangbi earthquake swarm occurred at the connection point of the dominant dextral strike-slip faults, namely the Red River fault and the Weiqi-Qiaohou fault, representing a different tectonic environment compared to the 2013 $M_W5.7$ Deqin earthquake swarm. This distinct setting suggests that either of these two faults could ~~may~~ be at risk of seismic activity during the pre-earthquake period of the upcoming earthquakes in this region.~~.~~

~~Due to t~~The high altitude, dense vegetation, and easily weathered conditions make it challenging to ~~,~~ obtain~~ing~~ accurate fault slip rates ~~poses a significant challenge~~, often ~~resulting~~ resulting in~~in~~ significant~~notable~~ uncertainties~~errors~~. However, r~~R~~ecent studies have provided fresh insights into slip rates and fault behaviors, offering the potential to enhance the precision of seismic hazard models. For instance, ~~determining the dextral slip rate of the Zhongdian fault has proven particularly difficult due to high error margins.~~ Wu et al. (2019) ~~Recent research has~~ evaluated the Holocene dextral slip rate of the Zhongdian fault to be ~1.5±0.2 mm/yr based on displacements of water-ice remains ~~(Wu et al., 2019)~~, while Chang et al. (2014) obtained ~~and~~ ~2.1±0.2 mm/yr based on displacements of river terraces ~~(Chang et al., 2014)~~, both utilizing Optically Stimulated Luminescence (OSL) dating. These values notably differ from the right-

lateral slip rate of 4--6 mm/yr estimated by Shen et al. (2001) based on gully displacements from the last glacial period, but are more aligned with the rates derived from GPS velocity data (Cheng et al., 2012). Incorporating these updated fault slip rates into regional seismic hazard models has the potential to greatly improve holds the promise of enhancing their accuracy and. Therefore, integrating these new slip rates into the regional seismic hazard model is crucial to ensure the reliability of the results.

Given the inherent challenges of fieldwork studies on fault activities, only a limited number of investigations have been conducted regarding seismic hazard analysis in the Northwest Yunnan regionNWYR. Among these studies, Zhou et al. (2004) conducted a micro-zonation of seismic hazards in the NWYR. They examined regional fault activities through field surveys and estimated the potential maximum magnitude of these faults. Their approach involved outlining polygons around the source faults to divide them into different potential seismic sources and calculating historical seismicity rates within these polygons. This methodology is widely employed in seismic hazard modeling in China, particularly in the national seismic hazard map of the China Seismic Ground Motion Parameters Zonation Map (CSGMPZM) (Gao et al., 2015). The CSGMPZM also utilized this methodology to assess potential maximum magnitudes and compute seismicity rates. However, their studies often did not integrate fault geometry models, especially fault segmentation modelsdata. Consequently, the fault geometry, including rupture length and area, may not be accurately linked to the magnitude of large earthquakes. Furthermore, it is crucial to recognize the potential

occurrence of multi-segment rupturing, which has not been documented in historical records. Similarly, seismicity rates were typically derived solely from historical earthquakes and were not synchronized with fault slip rates. Relying solely on historical earthquakes for seismicity rate calculations may lead to either overestimation or underestimation of seismic hazards.

In this article, we developed a regional seismic hazard model for the ~~Northwestern Yunnan Region (~~NWYR~~)~~, accounting for fault slip behaviors, the potential ~~occurrence offor~~ large earthquakes~~, and~~ including the likelihood of multi-segment ruptures. We initially developed fault segmentation models for the primary active faults in the ~~Northwestern Yunnan Region (~~NWYR~~)~~, drawing on recent geological research on fault segmentation and geological fault slip rates. Subsequently, we employed the SHERIFS code (Chartier et al., 2017; 2019) to simulate seismicity rates across possible multi-segment combination models. We identified the multi-segment combination model that best aligns with the majority of fault slip rates, considering fault segmentation and historical seismicity rates. ~~Ultimately, we calculated the Peak Ground Acceleration (PGA) with a 10% probability of exceedance within 50 years using the seismicity rates from the selected fault segmentation models.~~ Ultimately, we calculated the Peak Ground Acceleration (PGA) with a 10% probability of exceedance within 50 years using the seismicity rates from the selected fault segmentation models and the logic tree model of GMPEs analyzed to be suitable for China mainland. The exploration of multi-segment rupture combinations, along with the resultant modeled seismicity rates and

179 PGA values, offers valuable insights into the seismic hazard present in the NWYR. ~~By~~

180 ~~l~~Leveraging the modeled PGA values and accounting for the site response of different

181 rock type, we employed a machine learning model to compute the probability

182 distribution of landslides induced by potential seismic hazards. This increas~~ing~~~~ed~~

183 precision and reliability will be invaluable for guiding disaster preparedness initiatives,

184 land-use planning, and infrastructure resilience strategies in the area.

185

186
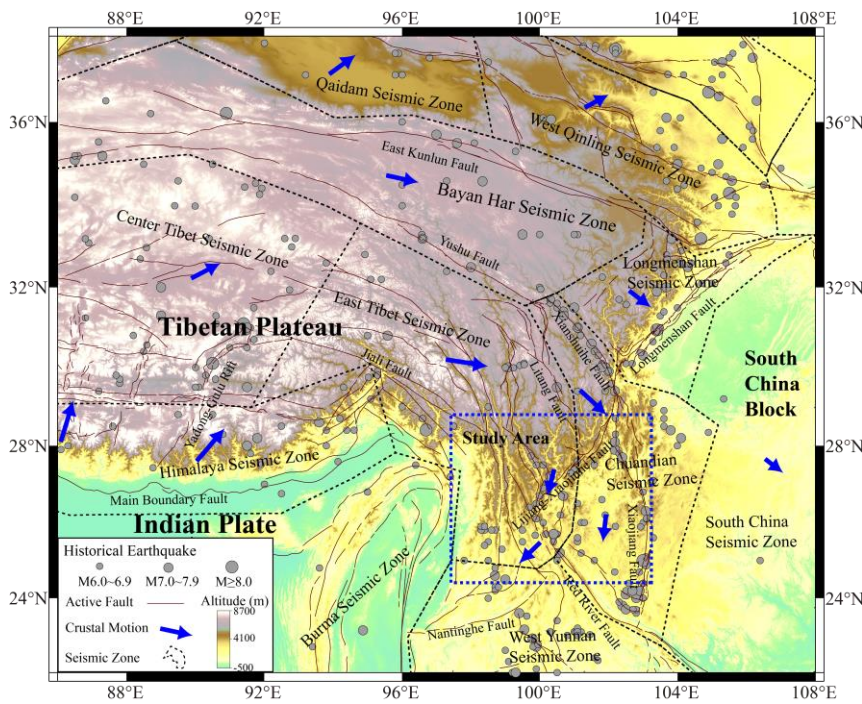
188 Figure 1. Tectonic environment of the Eastern Tibetan Plateau and the location of the

189 ~~Northwestern Yunnan Region (~~NWYR~~)~~. The dashed rectangle delineates the study area,

190 while dashed polygons depict the seismic zones delineated by Rong et al. (2020).

191

Figure 2. Regional active faults and historical earthquake activities in the NWYR. The focal mechanisms of recent earthquakes (1976~2023) are sourced from the global centroid moment tensor (GCMT) catalog. Earthquakes with M6+ are sourced from the moment magnitude (M_W) catalog of Cheng et al. (2017). The dashed line represents the division for background seismicity calculation, which extends 20 km from the faults. JP-Fau: Jinping fault; LT-Fau: Litang fault; ANH-Fau: Anninghe fault; ZMH-Fau: Zemuhe fault; XJ-Fau: Xiaojiang fault; CJ-Fau: Chuxiong-Jianshui fault; RR-Fau: Red River fault; NTH-Fau: Nantinghe fault; DYJ-Fau: Dayingjiang fault; NJ-Fau: Nujiang fault; LCJ-Fau: Lancangjiang fault; JSJ-Fau: Jinshajiang fault; ZD-Fau: Zhongdian fault; LX-Fau: Lijiang-Xiaojinhe fault; WQ-Fau: Weixi-Qiaohou fault; YLE-Fau: Yulong East fault; LQ-Fau: Longpan-Qiaohou fault; HE-Fau: Heqing-Eryuan fault; CH-Fau: Chenghai Fault; DCSE-Fau: Diancangshan East Fault; TW-Fau: Tongdian-Weishan Fault.

2. Fault slip rates, Segmentation, and Multi-segment Rupture Combinations Models

2.1 Fault slip rates, Segmentation

In the NWYR, the Lijiang-Xiaojinhe fault, characterized by its left-lateral strike-slip rate, and the northern section~~segment~~ of the Red River fault, ~~which displays~~known for its significant right-lateral strike-slip movement, play pivotal roles in crustal deformation. ~~Moreover, as a result of t~~While the southward crustal extrusion of the Tibetan Plateau enhances the left-lateral strike-slip of the ~~,~~ NE-trending faults like~~such as~~ the Lijiang-Xiaojinhe fault ~~also manifest a left-lateral strike-slip component~~. These observations underscore the complex interplay of fault dynamics in the NWYR, as elucidated by previous studies (Gan et al., 2007; Cheng et al., 2012; Wang and Shen, 2020).

To counterbalance the southwestward crustal extrusion (Wang et al., 1998; Cheng et al., 2012), several other faults in the region, such as the Chenghai fault, the Ninglang fault, the Heqing-Eryuan fault, the Yulong East fault, and the Longpan-Qiaohou fault (also known as the Jianchuan fault), also exhibit a component of normal slip rate as well (Institute of Geology-State Seismological Bureau, and Yunnan Seismological Bureau, 1990; Han et al., 2004) (see Figure 2). In contrast, the Zhongdian fault and the northern part of the Red River fault, including the Weixi-Qiaohou fault and the Diancangshan East fault, exhibit right-lateral strike-slip movement (Zhou et al., 2004; Han et al., 2005). Recent focal mechanisms of intermediate earthquakes indicate a complex regional

228 stress field, featuring both strike-slip and normal faulting regimes (Figure 2). Table S1

229 provides an overview of the observed fault slip rates in the NWYR.

230 The Lijiang-Xiaojinhe fault serves as a boundary fault ~~delineating~~ separating the

231 Tibetan Plateau from the Central Yunnan block (Xu et al., 2003; Cheng et al., 2012).

232 We divided the Lijiang-Xiaojinhe fault into 10 segments (the F1~F10 segments in

233 Figure 3) based on fault geometry and its intersection with other faults. For the F1

234 segment, known as the Jinpingshan fault, recent fault mapping reveals a Holocene left-

235 lateral slip rate ranging from 1.3~ to ~2.7 mm/yr derived from gully displacement across

236 the segment, while the vertical slip rate is approximately 0.2 mm/yr (Mr. Rui Ding,

237 2024, private communication).

238 Regarding the F5~F10 segments, Gao et al. (2019) demonstrated that the Hongxing-

239 Jianshanying segment (F6 segment in Figure 3) exhibited a Holocene left-lateral slip

240 rate of 3.32±0.22 mm/yr with a normal slip rate component of 0.35±0.02 mm/yr,

241 whereas the Runan-Nanxi segment (F10 segment in Figure 3) had a Holocene left-

242 lateral slip rate of 2.37±0.20 mm/yr. Accordingly, we applied the slip rate of the F6

243 segment ~~to~~for the F4~F7 segments, and the slip rate of the F10 segment ~~for~~to the

244 F8~F10 segments. Notably, we considered the strike-slip motion of the F5~F10

245 segments to originate from two sources: the strike-slip Jinpingshan fault and the strike-

246 slip of the Litang fault, aligning with the observed clockwise rotation of regional crustal

247 deformation around the Litang fault and the Lijiang-Xiaojinhe fault. Consequently, we

248 inferred the left-lateral strike-slip rate of the F4 segment to be ~2.1 mm/yr, consistent

249 with the southern section of the Litang fault (Zhou et al., 2007). However, the F2 and

250 F3 segments, which link the F1 and F4 segments, lack recorded fault slip rates from

251 fieldwork studies. In this regard, we assigned a conservative estimate, employing half

252 the value of the strike-slip rate of the F1 segment for both the F2 and F3 segments,

253 approximately 1.2 mm/yr.

254 For the Longpan-Qiaohou fault (comprising the F11~F14 segments), we delineated it

255 into four distinct segments based on the fault mapping data provided by Wu et al. (2023).

256 The sinistral slip rate of the Longpan-Qiaohou fault was estimated at ~2.2 mm/yr over

257 the past 3500 years, with a normal slip rate of 0.23 mm/yr (Institute of Geology-State

258 Seismological Bureau, and Yunnan Seismological Bureau, 1990).

259 As for the Yulong East fault, we ~~segmented~~ divided ~~the fault~~it into two segments,

260 namely the F15 and F16 segments, utilizing fault mapping data and Quaternary

261 sedimentary distribution. The slip rate of the Yulong East fault was assessed by Han et

262 al. (2005), who determined that the Quaternary left-lateral and normal slip rates are

263 0.84 mm/yr and 0.70 mm/yr, respectively, derived from the displacement observed in a

264 gully crossing the fault.

265 Regarding the Zhongdian fault, we partitioned it into six segments, designated as the

266 F17~F22 segments, based on fault mapping data (Wu et al., 2023). The Holocene

267 dextral slip rate of the Zhongdian fault is estimated to be approximately 1.7-2.0 mm/yr,

268 with a minor normal slip rate of 0.6-0.7 mm/yr based on terrace displacement across

269 the fault (Chang et al., 2014).

270 For the Heqing-Eryuan fault, we segmented it into two sections, labeled as the F23 and

271 F24 segments. The Quaternary dextral slip rate and normal slip rate of the Heqing-

272 Eryuan fault were reported to be around 2 mm/yr and 0.7-~1.0 mm/yr, respectively, as

273 documented by the Institute of Geology-State Seismological Bureau, and Yunnan

274 Seismological Bureau (1990). Additionally, recent research by Sun et al. (2017) yielded

275 similar fault slip rate results, indicating a left-lateral slip rate of 1.80 mm/yr and a

276 vertical slip rate of 0.28 mm/yr since the Pleistocene.

277 The Ninglang fault is primarily characterized as a left-lateral strike-slip fault, although

278 it exhibits a minor normal slip component of less than 0.1 mm/yr at the basin margin.

279 The strike-slip rate of the Ninglang fault, as determined from fault mapping work

280 conducted by Dr. Panxing Yang from Institute of Earthquake Forecasting, China

281 Earthquake Administration (2024, private communication), was estimated to be less

282 than 1 mm/yr. For our analysis, we opted to utilize a median value of 0.5±0.4 mm/yr

283 for the strike-slip rate of the Ninglang fault. Based on the distribution of Quaternary

284 sediments, we divided the Ninglang fault into two distinct segments, designated as the

285 F25 and F26 segments.

286 For the Chenghai fault, tThe sinistral slip rate of the Chenghai fault has been estimated

287 to range fromat 2.5 to 3.0 mm/yr, determined from the erosion rate of the Jinshajiang

288 River crossing the fault. Additionally, the normal slip rate is reported to be ~ between

289 0.7- and 1.0 mm/yr, assessed from the lift rate of the fault scarps (Institute of Geology-

290 State Seismological Bureau, and Yunnan Seismological Bureau, 1990), which is

291 consistent with the findings of Tang et al. (2017). We divided the Chenghai fault into

292 three segments, i.e., the Chenghai segment (the F27 segment), the Qina segment (the

293 F28 segment), and the Bingchuan segment (the F29 segment), based on the sedimentary

294 distribution (Huang et al., 2018; Yu et al., 2005).

295 The southern end of the Longpan-Qiaohou fault separates the Weixi-Qiaohou fault from

296 the Tongdian-Weishan fault. We segmented these two faults into six segments each

297 based on fault mapping data and Quaternary sedimentary distribution. Concerning the

298 slip rate of the Tongdian-Weishan fault, the dextral slip rate in the Late Pleistocene is

299 estimated to be ~1.8-2.4 mm/yr, with a normal slip rate of 0.17-0.35 mm/yr, calculated

300 from the displacement of fault scarps (Chang et al., 2016).

301 In contrast, for the Weixi-Qiaohou fault, the dextral slip rate is ~1.25 mm/yr, while the

302 normal slip rate is ~0.91 mm/yr since the Late Pleistocene (Ren et al., 2007). Comparing

303 these rates to the dextral slip rate from the middle section of the Red River fault, which

304 is reported to be 1.1 ± 0.4 mm/yr (Shi et al., 2018), it is evident that the dextral slip

305 rates decrease from the northwest to the southeast across the Red River fault system,

306 encompassing the Weixi-Qiaohou fault, the Tongdian-Weishan fault, and the Red River

307 fault.

308 The Diancangshan East Fault is the seismogenic fault of the 1925 M7 Dali earthquake.

309 We deduced that the Diancangshan East fault is a dominant normal slip fault as the

310 boundary fault of the Dali basin and the Erhai Lake. The normal slip rate of this fault is

311 1-2 mm/yr (Guo et al., 1984; Zhou et al., 2004).

312 Additionally, we incorporated the F37 and F38 segments of the northern part of the Red

313 River fault into our segmentation model. The right-lateral strike-slip rate of these two

314   segments is ~1.1 mm/yr. Figure 3 illustrated the segmentation model of the faults in the

315   NWYR.
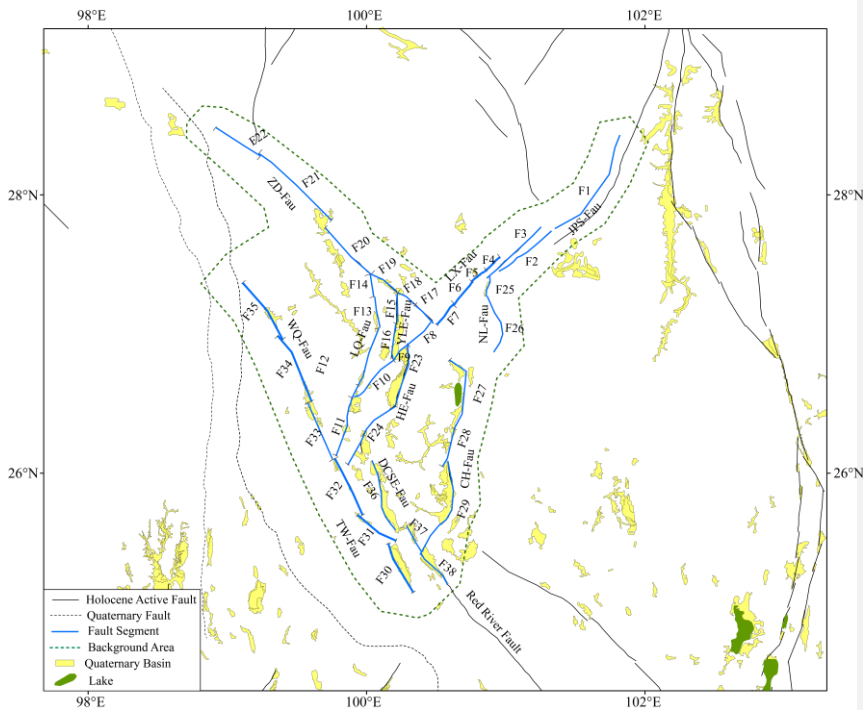
316

317   Figure 3. Fault segmentation model for the ~~Northwestern Yunnan Region (~~NWYR~~)~~.

318 In which, the Quaternary Basin distribution were from Deng et al. (2003); the fault

319 data are from Wu et al. (2023).

320

321 **2.2 Multi-segment Rupture Combinations Models**

322   Recently, geological and geophysical studies have documented several large

323 earthquakes characterized by multi-segment rupturing. Notable examples include the

324 M_W7.4 Landers earthquake in 1992 (Campillo and Archuleta, 1993), the M_W7.9

325 Wenchuan earthquake in 2008 (Xu et al., 2009), the M_W7.8 Kaikoura earthquake in

326 2016 (Xu et al., 2018), and the 2023 doublet events of M_W7.8 and M_W7.5 in Turkey

327 (Petersen et al., 2023). These events exhibited rupturing across different segments,

328 resulting in larger magnitudes than would be expected from single-segment ruptures.

329   Numerous studies have focused on understanding the fault's geometric and

330 physical parameters to ascertain conditions conducive to multi-segment rupturing.

331 Factors identified include step width (e.g., < 5 km) (Harris and Day, 1999; Lozos et al.,

332 2012), fault structural maturity characterized by initiation age, net slip, length, and slip

333 rate (Manighetti et al., 2007; 2021), and geometric irregularities such as fault branches

334 and bends, significantly influenced by the pre-existing stress field (Mignan et al.,

335 2015).For the strike-slip faults, we employed the conclusions of the step width of 5

336 km from dynamic rupture modelling (Harris and Day, 1999) and strike difference of 28°

337 + observed from fieldworks of historical rupture events (Biasi and Wesnousky, 2017)

338 can stop the earthquake rupture to select the multi-segment rupture combinations.

339

340   For strike-slip faults, we applied conclusions from dynamic rupture modeling,

341 indicating that a step width of more than 5 km (Harris and Day, 1999), and a strike

342 difference of more than 28°, as observed in field studies of historical rupture events

343 (Biasi and Wesnousky, 2017), could inhibit earthquake rupture, to select the multi-

344 segment rupture combinations.

345   In our segmentation model of the NWYR, the distance of the F3 segment and the

346 F1-F2 segments is ~7 km, while the width of step between the F20 and F21 segments

347 is also ~7 km. Similarly, the distance between the F3 segment and the F4 segment is

348 ~6.5 km. Thus, we did not consider the rupture continuities of these segments. For the

349 multi-fault rupture combinations, we can excluded almost all the multi-fault rupture

350 combinations.

In our segmentation model of the NWYR, the distance between the F3 segment and the F1-F2 segments is approximately 7 km, and the step width between the F20 and F21 segments is also about 7 km. Similarly, the distance between the F3 segment and the F4 segment is approximately 6.5 km. Based on these distances, we did not consider the rupture continuity of these segments. For multi-fault rupture combinations, the strike difference was also used to assess whether multi-fault rupture could occur. Consequently, we excluded nearly all the multi-fault rupture combinations, except for the combination between the F10 and F11 segments, which have a strike difference of about 20°.

Based on the segmentation model, fault rupture behaviors, and the intersections among fault segments, and geometric information discussed above, we developised four multi-segment rupture combination models for the fault segments in the NWYR (Figure 4). The M_W6.6 Lijiang earthquake on February 3, 1996, represents a significant normal rupture event that occurred on the Yulong East fault. This earthquake stands out as the most substantial seismic event in the NWYR since the 1970s, underscoring the normal slip behavior of the Yulong East fault. This observation suggests potential effect on the multi-segment ruptureimplications for the rupture behavior of the Zhongdian fault.

In Model 1, we exclusively examined the multi-segment rupture combinations within the same faults. Specifically, for the Zhongdian fault, we includedintegrated the multi-segment rupturing of the F17 and F18 segments, as well as the multi-segment rupturing of the F19 and F20 segments. This approach considered the normal slip behavior of the Yulong East fault (F15 and F16 segments) and its potential impact on

Quaternary sedimentary distribution between the F18 and F19 segments of the Zhongdian fault. Subsequently, in Model 2, we evaluated the plausibility of multi-segment rupturing occurring across the F17~F20 segments.

In the NWYR, the prevailing fault behavior is sinistral slip along the northeast-trending faults, a trend consistent with the observed clockwise rotation in regional crustal deformation (Cheng et al., 2012) and the presence of ductile low-crust flow (Zhang et al., 2022). The sinistral slip observed along the Longpan-Qiaohou fault may strongly impacted on~~hinder~~ the dextral slip occurring along the Weixi-Qiaohou fault, which extends from the Tongdian-Weishan fault, contributing to the decrease in dextral slip rates observed from the Weixi-Qiaohou fault to the Tongdian-Weishan fault. In Model 3, we integrated the multi-segment rupture combination of the Weixi-Qiaohou fault (the F33~F35 segments) and the Tongdian-Weishan fault (the F30~F32 segments).

In 2023, two earthquakes of $M_W7.8$ and $M_W7.5$ successively ruptured the East Anatolia fault region in Turkey (Xu et al., 2023; Petersen et al., 2023). The rupture of the first earthquake, with Mw7.8, initiated on the splay Narli fault and propagated bilaterally along the main East Anatolia fault (Liu et al., 2023). Consequently, we took into account the possibility of rupture propagation from one fault to another in our rupture combinations. Using Model 4, we investigated whether the rupture on the Lijiang-Xiaojinhe fault could propagate to the Longpan-Qiaohou fault. This consideration was prompted by similarities in the rupture behavior between the F11 segment of the Longpan-Qiaohou fault and the F10 segment of the Lijiang-Xiaojinhe fault (Table S1), along with a ~~minor~~ strike difference of ~20°, smaller than the threshold of 28° proposed by Biasi and Wesnousky (2017)~~in strike~~ to prohibit the rupture process~~(Table S1)~~.

400
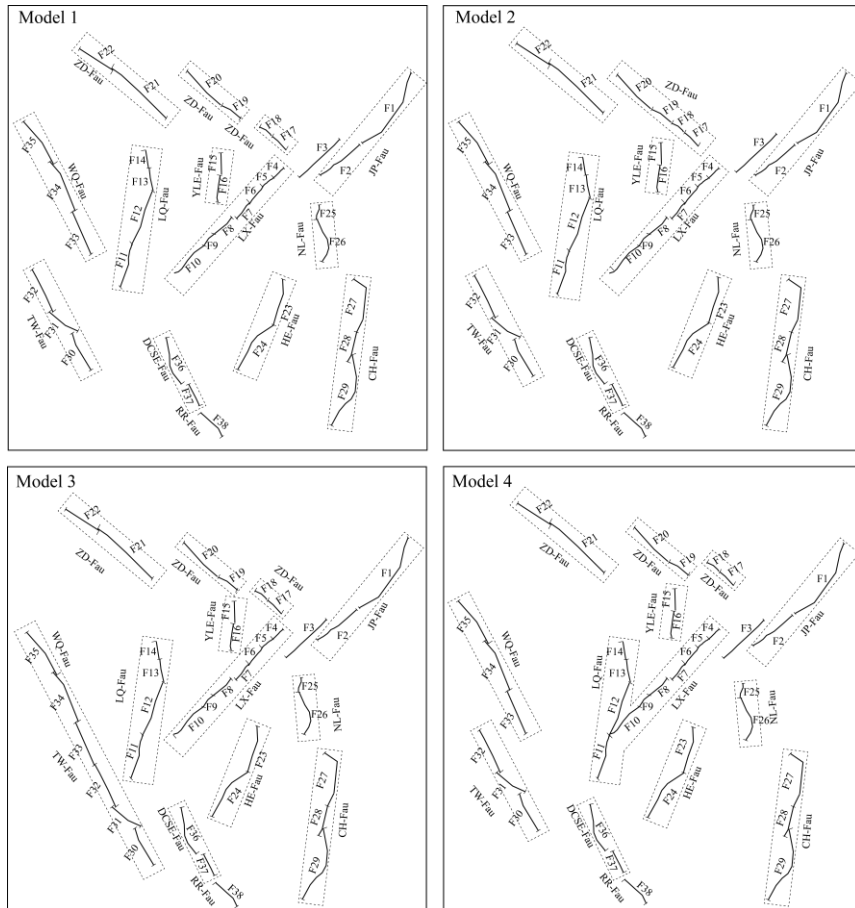
Figure 4 Possible Rupture Combination Models for the Fault Segments in NWYR.

Dashed rectangular show the rupture combinations for each Model.

403

3. Multi-segment rupture hazard Modeling

3.1 **Methodology:**

Recently, geological and geophysical studies have documented several large earthquakes characterized by multi-segment rupturing. Notable examples include the M_W7.4 Landers earthquake in 1992 (Campillo and Archuleta, 1993), the M_W7.9

409 Wenchuan earthquake in 2008 (Xu et al., 2009), the M_W7.8 Kaikoura earthquake in
410 2016 (Xu et al., 2018), and the 2023 doublet events of M_W7.8 and M_W7.5 in Turkey
411 (Petersen et al., 2023). These seismic events exhibited rupturing across different
412 segments, enhancing their overall magnitude and impact.

413 Numerous studies have focused on understanding the fault's geometric and
414 physical parameters to ascertain conditions conducive to multi-segment rupturing.
415 Factors identified include step width (e.g., < 5 km) (Harris and Day, 1999; Lozos et al.,
416 2012), fault structural maturity characterized by initiation age, net slip, length, and slip
417 rate (Manighetti et al., 2007; 2021), and geometric irregularities such as fault branches
418 and bends, significantly influenced by the pre-existing stress field (Kame et al., 2003;
419 Mignan et al., 2015).

420 Recognizing the importance of these rupture parameters in producing multi-
421 segment rupturing, recent studies, such as those by Chartier et al. (2019), Cheng et al.
422 (2021), Lee et al. (2022), and Chang et al. (2023), included the possibilities and
423 probabilities of multi-segment rupturing in seismic hazard analysis. Additionally,
424 Dutykh et al. (2013) and Rashidi et al. (2020) employed multi-segment rupturing into
425 models of tsunami wave generation. The concept of multi-segment rupturing was also
426 incorporated in the UCERF3 model through their complex "Grand Inversion"
427 methodology, which integrates data on fault slip rates, historical seismicity, and paleo-
428 earthquake records (Page et al., 2014; Field et al., 2014). However, for most other
429 regional studies, collecting all the necessary input parameters remains challenging.

430 In seismic hazard modeling, fault slip rates can be used instead of historical
431 seismicity data to simulate seismicity rates on faults, as slip rates span multiple seismic
432 cycles of large-magnitude earthquakes and provide estimates of the average earthquake
433 recurrence interval (Youngs and Coppersmith, 1985). W

Here, wWe utilized the methodology developed by Chartier et al. (2019) to translate these fault slip rates into seismicity rates, considering both multi-segment and single-segment ruptures.

3.1 Methodology

In the our earthquake hazard modeling, the seismicity rates should reflect both the fault slip rate and the regional magnitude-frequency distribution (MFD), e.g., the Gutenberg-Richter (G-R) Relationship (Gutenberg and Richter, 1944) and the Characteristic earthquake model (Schwartz and Coppersmith, 1984). Youngs and Coppersmith (1995) balanced fault slip rates with magnitude frequency relationshipMFD to determine the seismicity rate on faults. They employed the composite characteristic earthquake model (Y-C) or truncated G-R model to convert the fault slip rate into the seismicity rates on the fault. These converted MFD were widely used in seismic hazard analysis (e.g., Avital et al., 2018; Chartier et al., 2019; Rong et al., 2020). This approach enables a more comprehensive assessment of earthquake hazards by integrating both fault slip rates and the frequency of seismic events. For assessing the possibilities and probabilities of multi-segment rupturing, it is essential to represent the seismicity rate of such combinations within the magnitude-frequency relationship for each segment.

To achieve this, Chartier et al. (2017; 2019; 2021) devised a Python-based code known as SHERIFS. This code employed an iterative process, enabling the balancing of occurrence rates for multi-segment rupturing events alongside intermediate and small earthquakes on each fault segment (Figure 5a).

Leveraging historical seismicity data, they utilized the slip rate of each fault

segment to convert it into the target MFD on the fault, such as the G-R, or the Y-C distribution. This method offered a robust framework for assessing seismic hazard, integrating both single and multi-segment rupture scenarios effectively. Determining the maximum magnitudes of individual fault segments and their combinations could rely on fault length, following rupture scaling laws proposed by researchers (e.g., Wells and Coppersmith, 1994; Leonard et al., 2010; Cheng et al., 2020). Since ~~Most of the rupture scaling relationships are for Plate boundary regions and~~

~~Here, we selected the~~ most rupture scaling relationships are developed for plate boundary regions (Stirling et al., 2013), we selected a regression scaling relationship based on a dataset of earthquakes from China mainland (Cheng et al., 2020) and compared the results with those from the widely used rupture scaling relationship by Wells and Coppersmith (1994), which incorporates global data from both interplate and intraplate earthquakes.

In these steps, the b-value from historical earthquakes, the rupture scaling law of the faults, and the fault slip rates are typically accompanied by significant uncertainties. SHERIFS used the random sampling method to explore the uncertainty bounds. ~~For every branch of the logic tree, it generates a corresponding number of models, matching the total count of random samples.~~ The rates are derived while examining uncertainties related to earthquake magnitudes, the duration of the completeness period, and the limited number of observed earthquakes for larger magnitudes, using a Monte Carlo approach (Chartier et al., 2021). For each branch of the logic tree in the random sampling, it generates a corresponding number of models that match the total count of random samples. For each model, the slip-rate value is selected uniformly within its uncertainty bounds, scaling law parameters are chosen independently from a Gaussian

distribution within their error bounds, and the *b*-value is picked from the user-defined range. All these uncertainties propagate to the final step of calculating seismicity rates with uncertainties.

like Wells and Coppersmith (1994) and Cheng et al. (2020).

In the final step, they iterated the seismicity rates across magnitude bins associated with multi-segment rupturing, spanning from large magnitudes down to small magnitudes, according to the target MFD for each fault segment. However, in many cases, the fault slip rate or the calculated seismicity rates couldn't fully account for the entire seismic activity. The remaining portion of the fault slip rate for each segment was attributed to non-main-shock slip (NMS), including processes like post-seismic slip and silent creep. An NMS ratio of ≤30%-40% was typically considered indicative of a model misfit, potentially arising from factors like due to creeping and specific conditions, such as boundary fault segments or creeping segments (as depicted in Figure 5b). Here, we adopted a similar approach in simulating seismic hazard modeling for the regional fault system in the NWYR.
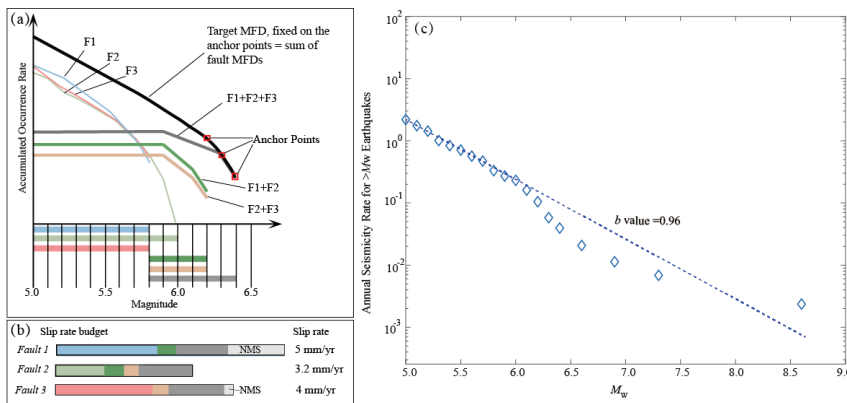
502
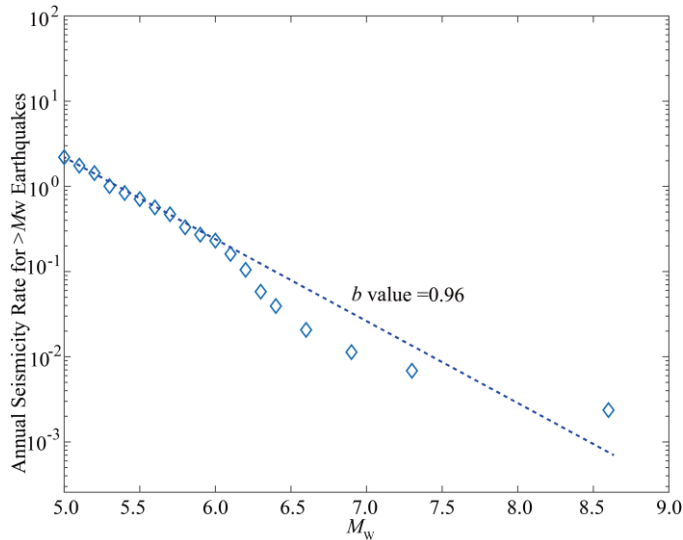
Figure 5 ~~a. Scheme of the occurrence rate iterative process on the fault segments~~

~~constrained by the magnitude-Frequency relationship and fault slip rates; b. Slip~~

~~budget of the fault slip rate and its consummation on the earthquakes (Modified from~~

~~Chartier et al., 2017); c.~~ Calculated b value for the East Tibet Seismic Zone where

the NWYR located in Figure 1.

3.2 Scaling Relationship and Modeling Parameters

Given the fractured structure of the crust in the NWYR, as documented by Cao et

al. (2023), the seismicity distribution in this area was notably complex and ~~differed~~

significantly _different_ from that observed directly on the fault lines. Therefore, in our

analysis of seismicity rates for ~~the whole seismicity rates on~~ the regional faults, we

opted to utilize the ~~Gutenberg-Richter (~~G-R~~)~~ relation (Gutenberg and Richter, 1944) as

the Magnitude-Frequency relationship, rather than the Youngs-Coppersmith (Y-C)

relation (Youngs and Coppersmith, 1985).

For estimating ~~the~~ magnitudes based on rupture length, we applied the ~~relationsip~~relationship proposed by Cheng et al. (2020) to determine the maximum magnitude for each individual fault segment as well as their multi-segment combinations. Additionally, we accounted for a portion of earthquakes with $M<6.5$ as off-fault seismicity. Specifically, we assigned probabilities of 95%, 90%, 85%, 80%, and 80% for magnitude bins ~~ranging from~~of 6.0 ~~to~~ 6.4, 5.5 ~~to~~ 5.9, 5.0 ~~to~~ 5.4, 4.5 ~~to~~ 4.9, and 4.0 ~~to~~ 4.4, respectively, based on prior studies (Chartier et al., 2019; Cheng et al., 2021).

We ~~conducted a~~ calculated ~~ion of~~ the b-value for the East Tibet Seismic Zone, which encompasses nearly all of the NWYR, as illustrated in Figure 1. The earthquake catalog utilized for this analysis was sourced from Cheng et al. (2017), covering the time period from 780 BC to 2015 AD. Additionally, we incorporated earthquakes from the Global CMT catalog spanning the period from 2016 to 2023 ~~into the dataset~~.

The regressed b-value was approximately 0.96, with completeness times for magnitudes $M_W4.5$, $M_W5.0$, $M_W5.3$, $M_W5.7$, $M_W6.1$, and $M_W6.4$ identified as 1985, 1966, 1928, 1916, 1916, and 1900, respectively. It is note~~'s~~worth~~y~~ ~~noting~~ that the calculated b-value is slightly higher than the value of 0.86 reported in Rong et al. (2020), likely due to the inclusion of new earthquakes occurring after 2015. Figure 5~~e~~ ~~provides a~~ visualiz~~es~~~~ation of~~the Gutenberg-Richter relationship in the East Tibet Seismic Zone, in which the b value is 0.96.

~~,~~

3.3~~2~~ Comparison and Selection of Modeled Results

We depicted the NMS ratios and modeled seismicity rates in Figure 6. The right

panels showcased the NMS ratios of the segments in Model 1~4. Model 1 exhibited the most balanced results between the modeled seismicity rates and historical ones. In Figure 6a, all segments in Model 1 demonstrated NMS ratios smaller than 30%. Chartier et al. (2019) suggested that NMS ratios below 30%-40% serve as a benchmark to assess the validity of multi-segment combination models, indicating effective consumption of the slip rate of each segment into seismicity rates ~~for each fault segment~~. The left panels in Figure 6b further underscored the alignment~~harmony~~ between the modeled and observed seismicity rates~~. Here~~, showing that the observed historical seismicity rates closely ~~aligned~~ matches~~with~~ the calculated rate~~ones~~, particularly for <M7 earthquakes.

Compared to Model 1, Model 2 ~~combined~~ treats segments F17~F20 as a single unit, rather than separating ~~instead of considering the~~ F17~F18 ~~segments~~ and ~~the~~ F19~F20~~ segments separately~~. The left panel of Figure 6b indicates that the NMS ratios for segments ~~of~~ F11~F14 and F4~F5 ~~are all greater than~~exceed 40%, while the F6~F7 multi-segment combination has an NMS ratio ranging from 30% to 40%, showing that the combination of segments F17~F20 has an obvious impact on the seismicity rates of these faults. From the right panel in Figure 6b, the historical seismicity rates for each fault segment were similar to those in Model 1. However, the calculated seismicity rates for each segment in Model 2 ~~became smalle~~were ~~r~~generally lower than those in Model 1, except for a slightly higher rate in the magnitude range of 6.0~6.5. This result indicated that the fault slip rates are not being adequately accounted for in Model 2, unlike in Model 1 (Figure 6a).

In Model 3, the rupture combination comprised segments of F30~F35, rather than

567 considering them separately as F30~F32 and F33~F35. Most segments exhibited high

568 NMS ratios in the left panel of Figure 6c. The calculated seismicity rates were generally

569 smaller than the historical ones in the right panel of Figure 6c. Similarly, Model 4 was

570 utilized to investigate whether the great earthquakes of the Y-shaped rupture, combining

571 segments F4~F10 with F11~F14, could occur. The NMS ratios for each segment and

572 the calculated seismicity rates were comparable to those observed in Model 3 (Figure

573 6d).

574

575   In addition, we also presented the results using the rupture scaling relationship

576 proposed by Wells and Coppersmith (1994) in Figure S1. Model 1 exhibited the most

577 consistent outcomes, with the maximum NMS ratio observed on F14 at 39.3%. The

578 NMS ratios for all other segments were below 30%. For the calculated seismicity rates

579 obtained from Model 2 to Model 4, using the rupture scaling relationship of Wells and

580 Coppersmith (1994), we observed similar patterns, with segments in aAll three models

581 exhibiting showed segments with NMS ratios exceeding 40%. FurthermoreIn summary,

582 we found that these models, utilizing the rupture scaling of Wells and Coppersmith

583 (1994), consistently yielded higher average NMS ratios on average compared to those

584 obtained from the rupture scaling of Cheng et al. (2020), though the ratios were similar.

585
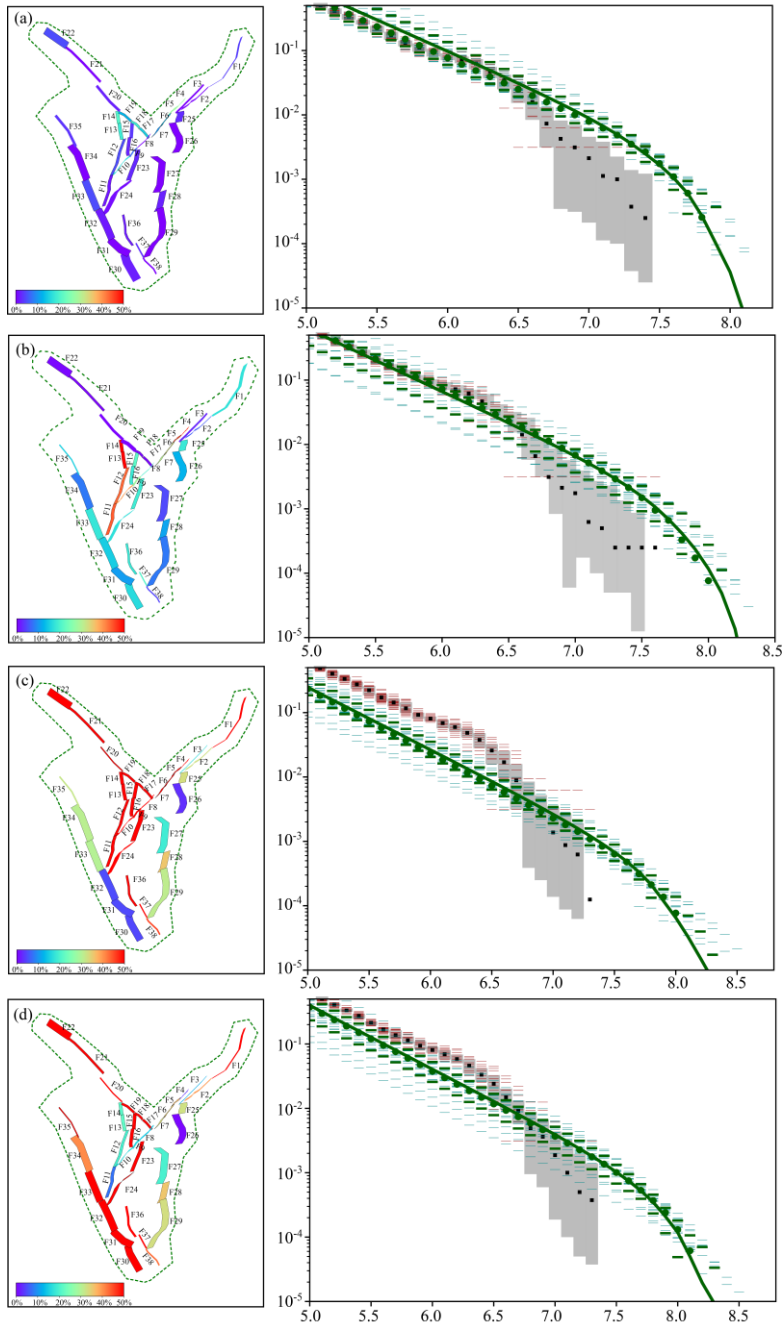
586
587 Figure 6 Calculated NMS ratios and comparison results for different models using the

G-R relation. (a) Modeled Non-Mainshock Slip (NMS) Ratio; (b) Comparisons between the historical Seismicity rates for different models. Dashed green lines are the MFD of each model, and the solid green line is the mean MFD, green patches represent the uncertainty (16-84 percentiles). The dotted black line is the rate from the catalog; the dashed red lines are individual Monte Carlo sampled rates of the catalog exploring the uncertainties on the magnitudes of earthquakes, and gray rectangular show the one-sigma uncertainty on the earthquake rates in statistical analysis.

Based on the comparison among different multi-segment rupture combination models, Model 1 demonstrated the most consistent results among the multi-segment rupture combinations, fault segment slip rates, and the Magnitude-Frequency relationship. Therefore, we utilized the seismicity rates from Model 1 to calculate the Peak Ground Acceleration (PGA) values for the NWYR. The output of the seismicity rates consist of 20

3.43 Comparison with the results Results of current Current national National Sseismic Hhazard Mmap Comparison with Current National Seismic Hazard Map Results

We utilized the OpenQuake Engine v3.10 (Pagani et al., 2014) to calculate the Peak Ground Acceleration (PGA) values for the NWYR. In this computation, we employed a logic tree model comprising the Abrahamson et al. (2014); Chiou and Youngs (2014); Campbell and Bozorgnia (2014); and Boore et al. (2014) branches of GMPEs, along with their associated uncertainties. Each branch was assigned an equal weight of 0.25, following the selection criteria established by Dangkua et al. (2018) for mainland China Mainland. These Ground Motion Prediction Equations (GMPEs) are

614 tailored for earthquakes characterized by moment magnitude (M_W) and the distance to

615 the rupture plane (Rrup) or its surface projection (R_{JB}).

616

617

618

619 Figure 7a illustrate~~sd~~ the distribution of ~~Peak Ground Acceleration~~ (PGA values~~)~~

620 for the site condition of firm to hard rock (Vs30=760 m/s, or NEHRP B) resulting from

621 the seismicity ~~model~~ rates in Model 1, corresponding to a 10% probability of

622 exceedance in 50 years, ~~which is~~ equivalent to a return period of 475 years. The analysis

623 revealed concentrations of high PGA values exceeding 0.40 g near fault sources,

624 particularly in areas with multiple fault sources. These areas include the F2~F5

625 segments of the Lijiang-Xiaojinhe fault, the vicinity of the Yulong East Fault (YLE-

626 Fau), the southern part of the Zhongdian fault (ZD-Fau), and the northern extent of the

627 Heqing-Eryuan fault (HE-Fau).

628

629 The area around~~of~~ the F2~F5 segments includes three parallel faults, with the sum

630 of the strike-slip of ~3 mm/yr, makes the PGA values relatively higher. The maximum

631 magnitude for~~of~~ the combinations of the F17~F18 ~~segments~~ and the F15~F16 segments

632 are both approximately M_W6.6. These areas exhibit a prevalence of moderate

633 earthquakes with short recurrence intervals and high ~~Peak Ground Acceleration~~ (PGA~~)~~

634 distributions over a 475-year return period. The modeled seismicity rates for both~~of~~ the

635 F23 ~~segment~~ and the F24 segments ~~both~~ complied with the G-R relationship, ~~containing~~

636 with sufficient~~enough~~ intermediate earthquakes, ~~induced~~ contributing to the high PGA

637 values in the surrounding areas~~around~~. Along the Chenghai fault, high PGA values are

638 concentrated ~~are also observed~~ around the F27~F28 segments with strike-slip rates of

639 3.0 mm/yr, but are lower around the F29 segments with a strike-slip rate of 2.5 mm/yr.

640 For the Red River fault and its extensions, including the Tongdian-Weishan fault and

641 the Weixi-Qiaohou fault, high PGA values are were concentrated around the F37~F38

642 segments and at the intersection points of the F11, F32, and F32 segments.

643

644 Compared toison with the national seismic hazard map of the China Seismic

645 Ground Motion Parameters Zonation Map (CSGMPZM) (Gao et al., 2015) (Figure 7b)

646 for the site condition of dense soil and soft rock (Vs30 = 500 m/s, or NHERP C) (Chen

647 et al., 2021), our Peak Ground Acceleration (PGA) values are consistently much higher

648 and more intricatedetailed. The Vs30 of 500 m/s is equivalent to the Type II in the

649 classification table of CSGMPZM, while the value of 760 m/s belongs to Type I_1. Table

650 1 presentswas the adjustment factors used by CSGMPZM for site amplification (Gao

651 et al., 2015). Even whenif we applied these site amplification adjustment factors to

652 convert our PGA values from type I_1 to type II, the PGA values would not change

653 obviously as the adjustment are closethe near to 1 for PGA values of 0.30—0.40 g, and

654 1 for PGA values of ≥0.40 g. In Ffigure 7b, the CSGMPZM indicates two high PGA

655 values ranging from 0.30 to 0.40 g in the NWYR, specifically around the F23~F24

656 segments and the F27~F28 segments, respectively. In contrast, the PGA values in other

657 areas surrounding the fault segments in our model range from 0.20 to 0.30 g.

658 In the development of the CSGMPZM, the region in the around China was divided

659 into 29 large seismic source zones to calculate the parameters of the Magnitude-

660 Frequency Distribution (MFD). Additionally, over 1,000 potential fault sources across

661 China were incorporated into the model. Historical seismicity rates on the MFD were

662 employed to predict future seismic activity. This methodology led to lower anticipated

663 seismicity rates in regions with limited historical earthquake records. The identification

Formatted: Subscript

664 of potential fault sources in the CSGMPZM relied on expert opinions gleaned from
665 research on historical surface rupture, fault segmentation, and the distribution of past
666 earthquakes. These data sources were subsequently utilized to allocate predicted
667 seismicity rates based on the MFD.

668 Furthermore, the utilization of different ~~Ground Motion Prediction Equations~~
669 ~~(GMPEs)~~ in the CSGMPZM compared to our results could also contribute to variations
670 in PGA values. The CSGMPZM utilized GMPEs from Yu et al. (2013) based on surface
671 magnitude (M_S) and epicentral distance (Repi). Their GMPEs result in higher PGA
672 values for distances less than 80 km but lower values for distances $\geq$80 km (Cheng et
673 al., 2021). Consequently, the seismicity rates derived from ~~the~~ fault slip rates and ~~the~~
674 multi-segment rupture combinations were key factors that re~~ndered~~sulted in our
675 modeled PGA values higher than those from CSGMPZM.
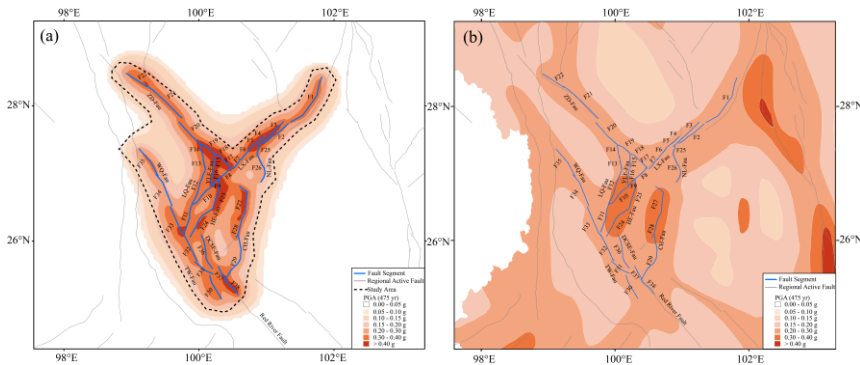
676
677 Figure 7 Comparison of the Modeled PGA distribution of 10% in the next 50 years,
678 (a) the PGA results in this article (b) the PGA results in the CSGMPZM.

679
680
681 Table 1 Adjustment factors for PGA values of different Site condition via Type II

PGA values for type II	Site condition type				
	I_0	I_1	II	III	IV
$\leq$0.05 g	0.72	0.80	1.00	1.30	1.25

0.10 g	0.74	0.82	1.00	1.25	1.20
0.15 g	0.75	0.83	1.00	1.15	1.10
0.20 g	0.76	0.85	1.00	1.00	1.00
0.30 g	0.85	0.95	1.00	1.00	0.95
≥0.40 g	0.90	1.00	1.00	1.00	0.90

682

3.5 Validity of ~~Our~~ the Modeled Results

684   In Figure 8, we further illustrated seismicity rates for several typical fault segments

685 to elucidate the reasons behind the observed high PGA values. ~~In~~ Figure 8a shows~~,~~

686 the seismicity rates of the F2 segment exhibit a typical G-R relationship, with a

687 sufficient number of intermediate earthquakes contributing ~~leading~~ to a high PGA

688 distribution in the surrounding area. We compared the seismicity rates on the F7~F8

689 segments~~,~~ and the F10 segment with the recurrence intervals from paleo-earthquake

690 studies. In Figures 8b and ~~~~8c, the ~~red~~ gray bars illustrate that our modeled seismicity

691 rates align with the recurrence interval of approximately 3000 years for a ~~magnitude~~

692 M_W7.5 earthquake, as ~~determined~~ reported by Ding et al. (2018).

693   We ~~have~~ also observed that segments F7 to F8 of the Lijiang-Xiaojinhe fault tend

694 to ~~conform to~~follow the characteristic earthquake model, based on their seismicity rate

695 distribution. The ~~Segment~~ F10 segment, ~~with a length of~~approximately 44 km in length,

696 ~~experienced~~ ruptured during the 1751 M6.8 earthquake. Additionally, Tang et al. (2014)

697 identified three paleo-earthquake events with a recurrence interval of ~~around~~ ~5300

698 years for earthquakes of M6.5+ earthquakes on the F11 segment ~~F11~~. They suggested

699 that the two paleo-events prior to the 1751 AD earthquake ~~before 1751 AD~~ were

700 considerably stronger ~~than the one in 1751 AD~~, implying multi-segment rupturing

701 involving combinations of segments F11+F12, F11~F13, and F11~F14 resulting in

702 magnitudes of M_W7.4~7.6 earthquakes. Additionally, we illustrate the seismicity rates

703 for~~on~~ segments F15, F27, F29, and F36 in Figures 8e~8f, which closely ~~resemble~~

704 follow the G-R distribution, leading to high PGA distributions in their vicinity. These

705 results demonstrate that the occurrence rate of intermediate earthquakes play a

706 significant role in driving~~influences~~ the high PGA distributions.

707

708
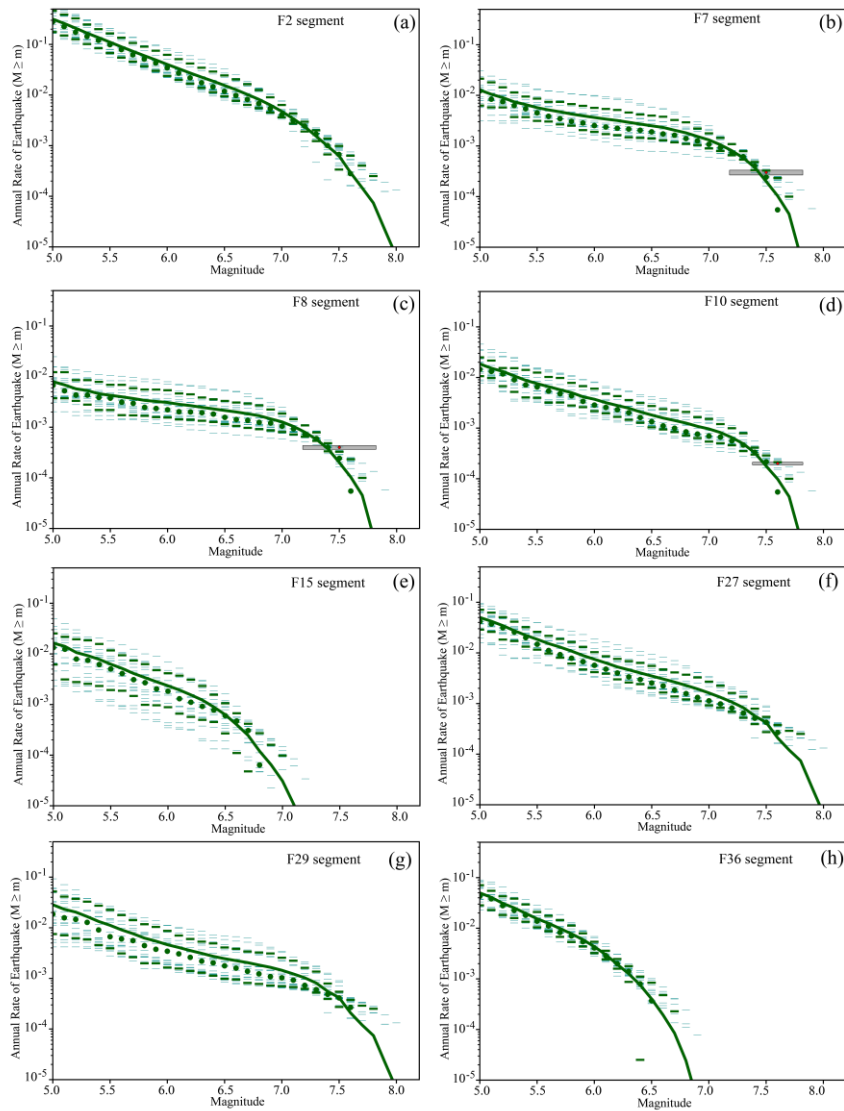
709
710 Figure 8 Modeled Seismicity rates for different magnitude on the fault segments. The

711 solid line is the mean MFD, and small patches represent the uncertainty (16-84

712 percentiles). The dotted line is the rate from the catalog with uncertainties. The red

713 circle is the occurrence rate of the repeated large historical earthquake rate, and the gray

714 box is the associated uncertainty.

3.64 Landslide Probabilities

3.6.1 PGA Site Amplification

Utilizing the modeled PGA values for rock site conditions presented in Figure 7a as a foundation, we enhanced our analysis by incorporating the site amplification effects derived from Chen et al.'s (2021) comprehensive site condition map. Their research, leveraging geological unit data, culminated in a detailed site condition map covering ~~mainland~~ China Mainland. Leveraging this invaluable resource, we integrated their site condition map along with the amplification factors for each geological type compared to type II (referenced in Table 1) to refine the PGA value distribution map (Figure 9a). Our methodology involved multiplying the PGA values for specific site conditions by the ratio of type II PGA values to those of the specific type. This approach effectively ~~magnified~~ amplified PGA values across different site conditions, enhanc~~rich~~ing the granularity of our analysis. Figure 9a illustrates the resultant PGA distribution map, now ~~encompassing~~ incorporates site amplifications specifically tailored for the NWYR region. Notably, our findings reveal minimal alterations in the PGA distribution, particularly ~~in proximity~~near ~~to~~ fault lines, where PGA values remain consistent or exceed 0.4 g (as detailed in Table 1).

3.6.2 Landslide Probabilities Derived from Modeled PGA Values

Using simulated ground motion data from potential earthquake scenarios, we conducted a thorough assessment of landslide susceptibility in the affected regions. Our analysis employed a machine learning framework, following the methodology outlined by Xu et al. (2019), to develop a predictive model for earthquake-induced landslides.

739 This model was trained utilizing data from nine earthquakes, ranging from the 1999

740 M_W7.7 Chichi earthquake to the 2017 M_W6.5 Jiuzhaigou earthquake, all of which

741 occurred within or near China. The training dataset comprised samples of earthquake-

742 induced landslides along withside 13 relevant factors. These factors encompassed

743 included variousdiverse parameters such as elevation, slope angle, slope aspect, land

744 cover, proximity to faults, geological characteristics, average annual rainfall, and PGA.

745 Leveraging this comprehensiverich dataset, we constructed developed a robust

746 predictive model capable of discerning assessing landslide probabilities.

747 (et al., 2020)

748 t

749 We used a logistic regression model, well-regarded for its robust performance in

750 machine learning. Unlike previous models (e.g., Nowicki et al., 2014; Wang and Rathje,

751 2015; Parker et al., 2017) for calculatingestimating earthquake-triggered landslide

752 hazards., oOour model directly assessed the absolute probability of landslide

753 occurrence. This probability is, represented as the percentage of the landslide area

754 within a given region relative to the total area of theat region (Shao et al., 2020).

755 This is represented as the percentage of the landslide area within a region relative

756 to the region's total area (Shao et al., 2020). As a result, our hazard estimates have a true

757 probabilistic meaning, reflecting the actual probability of landslide occurrence rather

758 than being merely serving as a formal expression of probability.

759 We then calculated the probabilistic seismic susceptibility for a specific point in

760 time within the study area, which producingeds a probabilistic seismic peak ground

761 acceleration (PGA) distribution map. By using this probabilistic PGA map as input for

762 our model, we can can estimate the corresponding probability of earthquake-triggered

763 landslide occurrence. We employed Tthesehis steps asforms the basis of our approach

to calculating the probability of such landslides.

Figure 9b illustrates the resultant landslide probability map for the NWYR region. Notably, areas ~~exhibiting~~ with high PGA distribution ~~correspond~~ closely correspond to regions with elevated landslide probabilities. For instance, notable areas include the northern end of the Zhongdian fault, the Jinpingshan fault, the Yulong East fault, the northern end of the Heqing-Eryuan fault, the northern part of the Chenghai fault, and the eastern section of the Lijiang-Xiaojinhe fault (the F2~F4 segments). Of particular significance are regions surrounding the Yulong East fault and the convergence zone of the Lijiang-Xiaojinhe fault and the Zhongdian fault. These areas exhibit pronounced differences in ~~altitude~~elevation, ample rainfall, and elevated PGA values, making them particularly susceptible to landslide occurrences.

By integrating multiple geospatial factors and leveraging advanced machine learning techniques, our analysis provides valuable insights into landslide susceptibility in earthquake-prone regions, aiding in effective risk management and mitigation strategies.
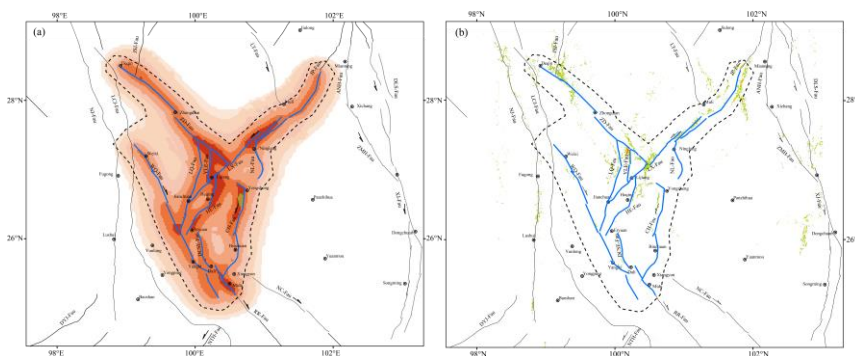
Figure 9. (a) PGA distribution Map considering different site amplifications; (b) the

784   probabilities of landslide occurrence impacted by the PGA values.

785

4 Discussion and Conclusion

787   In seismic hazard analysis, understanding fault behaviors, such as slip rates and geometries, is crucial for accurately modeling future seismic activity rates. Concurrently, historical earthquake occurrence rates provide a foundational basis for estimating these future rates. Notably, attention must also be given to earthquakes involving multi-segment ruptures, which may not be fully documented in historical records. In this article, we introduce a new seismic hazard model for NWYR, where the Tibetan Plateau boundary intersects with local low-crustal flow.

4.1 Model Limitations and ~~Corresponding~~Mitigation Measures

795   Our seismic hazard modeling for NWYR represents our current understanding of average earthquake hazards in the region based on available data. The results are affected by ~~numerous~~various epistemic and aleatory uncertainties inherent in seismic hazard modeling processes, including the MFD, fault geometry, fault type, slip rate, and variability in GMPEs. ~~Mitigating~~Addressing the impact of these uncertainties is cruc~~ial~~itical for ~~accurate~~ensuring accurate seismic hazard assessments.

802   The MFD relationship, calculated from historical earthquakes, is essential for determining seismicity rate ratios across different magnitude bins. Variations in the MFD ~~will~~ directly influence~~s~~ the distribution of the modeled seismicity rates. In this study, we chose the G-R relationship over the Y-C relationship due to the regional fragmented tectonic environment. The calculated b-value of 0.96 aligns closely with the expected value of 1 found in seismically active regions (Pacheco et al., 1992).

To deriveestimate earthquake magnitudes on fault segments, we employed rupture scaling relationships based on historical rupture parameters of earthquakes in China Mainland, as proposed by Cheng et al. (2020), ensuring consistency with unique tectonic characteristics. Achieving more precise MFDs and rupture scaling laws necessitates further refinement in methodology and the use of reliable catalogs specific to the study area. Achieving more accurate MFDs and rupture scaling laws will require further methodological refinement and the use of reliable, region-specific earthquake catalogs.

For fault geometry, type, and slip rates, we relied exclusively on recent field investigation data. In compiling fault rupture models for NWYR, we analyzed these geological data under a unified tectonic stress field, ensuring coordinated fault system movements. The variability in GMPEs is complex, influenced by factors such as earthquake rupture characteristics, seismic wave propagation, and site conditions. Consequently, we incorporated Quaternary sediment site amplification effects on PGA values. Addressing basin effects on ground motion requires dynamic simulations to achieve more precise results.

4.21 Multi-segment Rupturing Hazards in NWYR

The complex fault system results in earthquake occurring almost all the faults with various rupture behaviors in the NWYR, while the catalog of historical and paleo-earthquake data only recorded a small portionart of these rupturing events. The NWYR serves as the boundary region between China and Myanmar. This area is predominantly inhabited by ethnic minorities in China, resulting in limited written documentation of its history, particularly regarding earthquake disasters.

NeverthelessHowever, some significant earthquakes have been documented, particularly those that have had a seismic impacted on major cities like Dali, e.g., the 1515 *M*7.8 Yongsheng earthquake in Yongsheng ruptured two continuous linked segments of the Chenghai fault (Institute of Geology-State Seismological Bureau and Yunnan Seismological Bureau, 1990). The historical earthquake catalog used in our seismic hazard modeling often struggles fails to include all possible these combinations of ruptured scenarios that occurred in the past. To address this, What we have done is to searchexplored reasonable models for potential for possible rupture combinations and calculate their seismicity rates to include in our model.

These rupture combinations might be constrained by various factors, such as the geometry of fault segments, the width of the step-over between each pair of segments, and the maturity of the fault steps (Cunningham and Mann, 2007; Biasi and Wesnousky, 2017). For strike-slip faults, a step-over width of 5 km is often used to assess the reasonablenessplausibility of the rupture combinations (e.g., Biasi and Wesnousky, 2017). However, in the NWYR, where faults are situated withlocated in the a conduit of ductile low-crust flow, all step-overs are less than have 5 km wide,ths of less than 5 km except for the approximately the one of ~7 km step-over between the F20 and F21 segments. Hence, we advocate that the intersection relationship between faults is the primary determinant of whether multi-segment rupture events occur among fault segments in this region.

4.32 Implication of the small-block rotation in NWYR

The Holocene strike-slip motion of the Lijiang-Xiaojinhe fault behaves plays athe dominant role in this region, and intersecting boths the Heqing-Eryuan fault and the

Yulong East fault. Model 1 also confirm~~ed~~s the capability of the entire rupture of the F4~F10 segments of the Lijiang-Xiaojinhe fault. Additionally, the Lijiang-Xiaojinhe fault separates T~~t~~he Chenghai fault from~~and~~ the Zhongdian fault ~~also are separated by the Lijiang-Xiaojianghe fault~~, challenging ~~which differs~~ the view of Wang et al. (1998) that the Dali fault ~~(~~including the Longpan-Qiaohou fault and the Chenghai fault~~)~~ is the primary fault in this region. The Longpan-Qiaohou fault obstructs the westward continuation of the Lijiang-Xiaojinhe fault, and simultaneously, the F11 segment also resists rupturing in conjunction with the Lijiang-Xiaojinhe fault (Model 4 in Figure 4). In contrast, the Weixi-Qiaohou fault (WQ-F) and the Tongdian-Weishan fault (TW-F) belong to ~~are part of~~ distinct small-blocks and therefore cannot rupture simultaneously, as dep~~i~~ected in Figure 10a. This indicates that the northern end of the Red River fault is intercepted by the Longpan-Qiaohou fault. In our model, t~~T~~he Zhongdian fault (ZD-F) is~~was~~ separated for~~to~~ rupture ~~in our model~~ (Model 1 in Figure 4), ~~especially~~ particularly for the F17~F18 segments combination and the F19~F20 segments combination. ~~Here, w~~We propose that the normal- and strike-slip of the Yulong East fault poses a greater destructive potential to the Zhongdian fault compared to the strike-slip of the Longpan-Qiaohou fault.

Hence, our ~~configurations of~~ multi-segment rupture configuration~~s~~s portrayed in Model 1 of Figure 4 ~~correspond~~ align with~~to~~ the rotational patterns noted in the small block delineated in the NWYR by Wang et al. (1998). We illustrate~~d~~ this clockwise rotation of the small blocks in the NWYR in Figure 10a. This clockwise rotation i~~wa~~s further supported by GPS observations to the west of the Xianshuihe fault, the Anninghe fault, and the Xiaojiang fault, after ~~eliminating~~ removal of the entire movement (Figure 10b) (Cheng et al., 2012).

881   In Figure 10b, the area where the Nujiang fault intersects with the Dayingjiang

882 fault experiences the strongest extensional forces. Rangin et al. (2013) and Lindsey et

883 al. (2023) proposed that the dynamic source of this extensional tectonic environment

884 was the side effect of the gravitational collapse of the Tibetan Plateau with the

885 westwards of upper crust faster than the lower crust (Rangin et al., 2013; Lindsey et al.,

886 2023). This extensional force significantly affects~~exerts obviously on~~ the faults in our

887 model, driv~~mak~~ing the rotation of small blocks, and the normal slip of the regional

888 faults, e.g., the Diancangshan fault and the Chenghai fault.
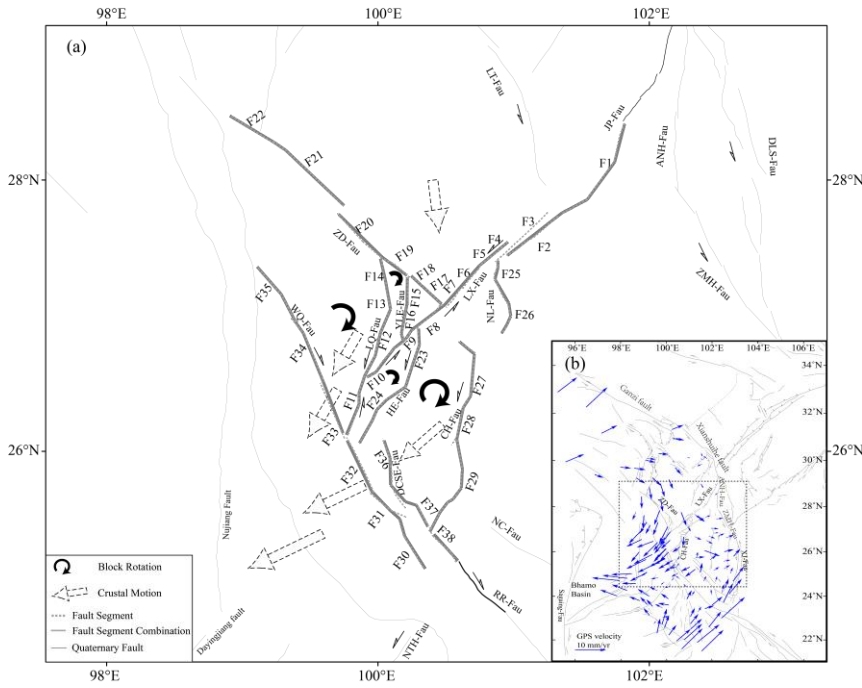
889

890   Figure 10 a. Kinematic Model of the faults in the NWYR; b. Regional GPS

891   motion after removing the whole movement (Cheng et al., 2012).

892

4.4 Conclusions

In conclusion, our study has provided valuable insights into the seismic hazard present in the NWYR. By developing fault segmentation models based on recent geological research and utilizing advanced simulation techniques, we have enhanced our understanding of fault activities and seismicity rates across the region. This study presents a comprehensive seismic hazard model for the NWYR, integrating fault slip rates and historical seismicity data to evaluateassess the risks of multi-segment ruptures and landslide occurrences. By leveraging fault slip rates and fault geometrical distributions in the NWYR, we employed the iterativesimulation method within the SHERIFS code to simulatecalculate seismicity rates for both single-segment and multi-segment ruptures. This work underscoreshighlights the complexity of the fault systems within the region's block rotational tectonic environment. Our study provideshas yielded valuable insights into the seismic hazards present in the NWYR. Through the development of fault segmentation models based on recent geological research and the application of advanced simulation techniques, we have significantly enhanced our understanding of fault activity and seismicity rates across the region. Through careful analysis and consideration of fault segmentation, fault slip rates, and historical seismicity, wWe alsohave identified multi-segment models that best represent the observed data.

Our calculations of PGA with a 10% probability of exceedance within 50 years offer crucial essential information for assessing seismic risk in the NWYR. The PGA values, associated with obvious latitude difference and, abundant precipitation, increase the likelihoodare prone to occurrence of landslides.

Furthermore, our investigation into multi-segment rupture combinations has

918 illuminated potential scenarios for seismic events in the region. By~~Through the~~

919 integration ~~of~~ these findings, we have generated a more comprehensive assessment of

920 seismic hazards and landslide probabilities. These factors are intertwined with the

921 regional small block rotation induced by the low-crustal flow and gravitational collapse

922 along the southeastern frontier of the Tibetan Plateau.

923

924 Future seismic hazard work can be improved by utilizing geophysical data to

925 understand fault structures where strong earthquakes are developing (Xu et al., 2017),

926 applying geodetic data to assess energy accumulation on fault segments (e.g., Yao and

927 Yang, 2023), using microseismicity relocation data to reveal fault asperities (Lay and

928 Nishenko, 2022), and employing dynamic rupture simulations of single and multi-

929 segments to enhance earthquake motion predictions (e.g., Zhang et al., 2017). These

930 studies on fault behaviors, interactions, and multi-segment ruptures are vital for

931 ~~improving~~enhancing seismic hazard assessments. Staying vigilant and proactive in

932 seismic risk management will better protect communities and infrastructure in the

933 NWYR and beyond.

934

935

Code availability

937 In this study, we have used the code related to Chartier et al. (2019,

938 https://doi.org/10.1785/02201803320), which can be downloaded from the webpage

939 (https://doi.org/10.1785/02201803320, last accessed in May, 2024).

940

Data availability

The focal mechanism data are from Global CMT catalog (www.globalcmt.org, last accessed in May, 2024) Table S1 in the supplementary material for this paper includes the fault segments, historical and paleo-earthquakes and their associated slip parameters.

Author contributions.

Jia Cheng was responsible for methodology, software, and writing the original draft. Chong Xu worked for the landslide occurrence probabilities calculation. Xiwei Xu and Shimin Zhang contributed to design the fault rupture combination models. Pengyu Zhu contributed to seismic hazard modeling.

Competing interests.

The authors declare that they have no known competing financial interests or personal relationships that could have appeared to influence the work reported in this paper.

Acknowledgments.

We thank Dr. Guangwei Zhang from National Institute of Natural Hazards and Dr. Mingming Jiang from Institue of Geology and Geophysics, Chinese Academy of Sciences for discussion on the dynamic source of the crustal deformation. We are also grateful to Mr. Rui Ding from National Institute of Natural Hazards and Dr. Panxing Yang from Institute of Earthquake Forecasting, China Earthquake Administration for their assistance in delineating fault traces and the fault segmentation work.

Financial support.

This study receives funds from the National Natural Science Foundation of China (No. U2039201 and No. 42074064), and National Institute of Natural Hazards, Ministry of Emergency Management of China (Grant NO. ZDJ2020-14).

968
969

References

Abrahamson, N., Silva, W., and Kamai, R.: Summary of the ASK14 Ground Motion Relation for Active Crustal Regions, Earthquake Spectra, 30, 1025-1055, 2014.

Avital, M., Kamai, R., Davis, M., and Dor, O.: The effect of alternative seismotectonic models on PSHA results – a sensitivity study for two sites in Israel, Nature Hazards and Earth System Sciences, 18, 499-514, 2018.

Bao, X., Sun, X., Xu, M., Eaton, D., Song, X., Wang, L., Ding, Z., Mi, N., Li, H., Yu, D., Huang, Z., and Wang, P.: Two crustal low-velocity channels beneath SE Tibet revealed by joint inversion of Rayleigh wave dispersion and receiver functions, Earth and Planetary Science Letters, 415, 16-24, 2015.

Biasi, G., and Wesnousky, S.: Bends and ends of surface rupture, Bulletin of Seismological Society of America, 107, 2543-2560, 2017.

Boore, D., Stewart, J., Seyhan, E., and Atkinson, G.: NGA-West2 Equations for Predicting PGA, PGV, and 5% Damped PSA for Shallow Crustal Earthquakes, Earthquake Spectra, 30, 1057-1085, 2014.

Campbell, K., and Bozorgnia, Y.: NGA-West2 ground motion model for the average horizontal components of PGA, PGV, and 5% damped linear acceleration response spectra, Earthquake Spectra, 30, 1087-1115, 2014.

Campillo, M., and Archuleta, R.: A rupture model for the 28 June 1992 Landers, California, Earthquake, Geophysical Research Letters, 20, 647-650, 1993.

Cao, Y., Jin, M., Qian, J., Chen, J., and Anyiam, U.: Crustal structure and seismicity characteristics based on dense array monitoring in northwestern Yunnan, China, Physics of the Earth and Planetary Interiors, 340, https://doi.org/10.1016/j.pepi.2023.107047, 2023.

994 Chang, Z., Zhang, Y., Li, J., and Zang, Y.: The Geological and Geomorphic
995   Characteristic of Late Quaternary Activity of the Deqin-Zhongdian-Daju Fault,
996   Journal of Seismological Research, 37, 46-52, 2014 (in Chinese with English
997   abstract).

998 Chang, Z., Chang, H., Zang, Y., and Dai, B.: Recent active features of Weixi-Qiaohou
999   fault and its relationship with the Honghe fault, Journal of Geomechanics, 22, 517-
1000   530, 2016 (in Chinese with English abstract).

1001 Chang, C., Chang, C., Gao, J., and Chan, C.: Quantifying the probability and
1002   uncertainty of multiple-structure rupture for Taiwan, Terretrial, Atmospheric, and
1003   Oceanic Sciences, 34, https://doi.org/10.1007/s44195-023-00040-9, 2023.

1004 Chartier, T., Scotti, O., Lyon-Caen, H., and Boiselet, A.: Methodology for earthquake
1005   rupture rate estimates of fault networks: example for the western Corinth rift,
1006   Greece, Nature Hazards and Earth System Sciences, 17, 1857-1869, 2017.

1007 Chartier, T., Scotti, O., and Lyon-Caen, H.: SHERIFS: Open-Source code for
1008   computing earthquake rates in fault systems and constructing hazard models,
1009   Seismological Research Letters, 90, 1678-1688, 2019.

1010 Chartier, T., Scotti, O., Lyon-Caen, H., Richard-Dinger, K., Dieterich, J. H., and Shaw,
1011   B.: Modelling earthquake rates and associated uncertainties in the Marmara
1012   Region, Turkey, Nature Hazards and Earth System Sciences, 21, 2733-2751, 2021.

1013

1014 Chiou, B., and Youngs, R.: Update of the Chiou and Youngs NGA Model for the
1015   Average Horizontal Component of Peak Ground Motion and Response Spectra,
1016   Earthquake Spectra, 30, 1117-1153, 2014.

1017 Chen, G., Magistrale, H., Rong, Y., Cheng, J., Binselam, A., and Xu, X.: Seismic site
1018   condition of Mainland China from Geology, Seismological Research Letters, 92,

998-1010, 2021.

Cheng, J., Xu, X., Gan, W., Ma, W., Chen, W., and Zhang, Y.: Block model and dynamic implication from the earthquake activities and crustal motion in the southeastern margin of Tibetan plateau, Chinese Journal of Geophysics, 55, 1198-1212, 2012 (in Chinese with English abstract).

Cheng, J., Rong, Y., Magistrale, H., Chen, G., and Xu, X.: An Mw-based historical earthquake catalog for mainland China, Bulletin of Seismological Society of America, 107, 2490-2500, 2017.

Cheng, J., Rong, Y., Magistrale, H., Chen, G., and Xu. X.: Earthquake rupture scaling relations for mainland China, Seismological Research Letters, 91, 248-261, 2020.

Cheng, J., Chartier, T., and Xu. X.: Multisegment Rupture Hazard Modeling along the Xianshuihe Fault Zone, Southeastern Tibetan Plateau, Seismological Research Letters, 92, https://doi.org/10.1785/0220200117, 2021.

Cunningham, W., and Mann, P.: Tectonics of Strike-Slip Restraining and Releasing Bends, Geological Society, London, Special Publications, 290, 1-12, 2007.

Dai, C., Gan, W., Li, Z., Liang, S., Xiao, G., Zhang, K., and Zhang, L.: Characteristics of Regional GPS Crustal Deformation before the 2021 Yunnan Yangbi Ms 6.4 Earthquake and Its Implications for Determining Potential Areas of Future Strong Earthquakes, Remote Sensing, 15, https://doi.org/10.3390/rs15123195, 2023.

Dangkua, D., Rong, Y., and Magistrale, H.: Evaluation of NGA-West2 and Chinese Ground-Motion Prediction Equations for Developing Seismic Hazard Maps of Mainland China, Bulletin of Seismological Society of America, 108, 2422-2443, 2018.

Deng, Q., Zhang, P., Ran, Y., Yang, X., Min, W., and Chu, Q.: Basic characteristics of active tectonics of China, Science China Earth Sciences, 46, 356-372, 2003.

Ding, R., Ren, J., Zhang, S., Lu, Y., and Liu, H.: Late Quaternary Paleoearthquakes on the Middle segment of the Lijiang-Xiaojinhe fault, Southeastern Tibet, Seismology and Geology, 40, 622-640, 2018 (in Chinese with English abstract).

Dutykh, D., Mitsotakis, D., Gardeil, X., and Dias, F.: On the use of the finite fault solution for tsunami generation problems, Theoretical and Computational Fluid Dynamics, 27(1-2), 177-199, 2013.

Field, E., Arrowsmith, R., Biasi, G., Bird, P., Dawson, T., Felzer, K., Jackson, D., Johnson, K., Jordan, T., Madden, C., Michael, A., Milner, K., Page, M., Parsons, T., Powers, P., Shaw, B., Thatcher, W., Weldon, R., and Zeng, Y.: Uniform California Earthquake Rupture Forecast, version 3 (UCERF3)—The time-independent model, Bulletin of Seismological Society of America, 104(3), 1122-1180, 2014.

Gan, W., Zhang, P., Shen, Z., Niu, Z., Wang, M., Wan, Y., Zhou, D., and Cheng, J.: Present-day crustal motion within the Tibetan Plateau inferred from GPS measurements, Journal of Geophysical Research: Solid Earth, 112, https://doi.org/10.1029/2005JB004120, 2007.

Gao, M., Li, X., Xu, X., Wei, K., Yu, Y., Zhou, B., Zhao, F., Pan, H., Lv, Y., and Zhou, Q.: GB18306-2015: Introduction to the Seismic Hazard Map of China, Standards Press of China, Beijing, 1-133, 2015 (in Chinese).

Gao, Y., Ding, R., Zhang, S., and Ren, J.: Slip rate of Lijiang-Xiaojinhe fault in the Holocene, Technology for Earthquake Disaster Prevention, 14, 617-627, 2019 (in Chinese with English abstract).

Guo, S., Zhang, J., Li, X., Xiang, H., Chen, T., and Zhang, G.: Fault displacement and

1069 recurrence intervals of earthquakes at the northern segment of the Honghe fault

1070 zone, Yunnan Province, Seismology and Geology, 6, 1-12, 1984 (in Chinese with

1071 English abstract).

1072 Gutenberg, B., and Richter, C.: Frequency of earthquakes in California,- Bulletin of

1073 Seismological Society of America, 34, 185-188, 1944.

1074 Han, Z., Guo, S., Xiang, H., Zhang, J., and Ran, Y.: Seismotectonic Environment of

1075 occurring the February 3, 1996 Lijiang M=7.0 earthquake, Yunnan Province, Acta

1076 Seismologica Sinica, 26, 410-418, 2004 (in Chinese with English abstract).

1077 Han, Z., Xiang, H., and Guo, S.: Sinistral shear and extension of the northern section

1078 of Lijiang Basin in northwest Yunnan in Quaternary, Chinese Science Bulletin, 50,

1079 452-459, 2005.

1080 Harris, R., and Day, S.: Dynamic 3D simulations of earthquakes on En Echelon Faults,

1081 Geophysical Research Letters, 26, 2089-2092, 1999.

1082 Huang, X., Wu, Z., Huang, X., and Luo, R.: Tectonic Geomorphology constrains on

1083 Quaternary Activity and Segmentation along Chenghai-Binchuan Fault zone in

1084 Northwest Yunnan, China, Earth Science, 43, 4651-4670, 2018 (in Chinese with

1085 English abstract).

1086 Huang, X., Wu, Z., Liu, F., Tian, T., Huang, X., and Zhang, Y.: Tectonic interpretation

1087 of the main paleoseismic landslides and their distribution characteristics in the

1088 Chenghai fault zone, Northwest Yunnan, Earth Science Frontiers, 28, 125-139,

1089 2021 (in Chinese with English abstract).

1090 Huang, P., Gao, Y., and Xue, B.: Advances in the deep tectonics and seismic anisotropy

1091 of the Lijiang-Xiaojinhe fault zone in the Sichuan-Yunnan Block, Southwestern

1092 China, Earthquake Research Advances, 2,

1093 https://doi.org/10.1016/j.eqrea.2022.100116, 2022.

Institute of Geology-State Seismological Bureau, and Yunnan Seismological Bureau.: Active faults in Northwestern Yunnan Region, Seismological Press, Beijing, China, 1-304, 1990 (in Chinese with English abstract).

Lay, T., and Nishenko, S.: Updated concepts of seismic gaps and asperities to assess great earthquake hazard along South America, 119, https://doi.org/10.1073/pnas.2216843119, 2022.

Lee, Y., Hui, Z., Daneshvaran, S., Sedaghati, F., and Graf, W.: Impacts on catastrophe risk assessments from multi-segment and multi-fault ruptures in the UCERF3 model, Earthquake Spectra, 38, 128-151, 2022.

Leonard, M.: Earthquake Fault Scaling: Self-Consistent Relating of Rupture Length, Width, Average Displacement, and Moment Release, Bulletin of Seismological Society of America, 100(5A), 1971-1988, 2010.

Lindsey, E., Wang, Y., Aung, L., Chong, J., Qiu, Q., Mallick, R., Feng, L., Aung, P., Tin, T., Min, S., Bradley, K., Than, O., Oo, K., Thant, M., Masson, F., Bürgmann, R., and Hill, E.: Active subduction and strain partitioning in western Myanmar revealed by a dense survey GNSS network, Earth and Planetary Science Letters, 622, https://doi.org/10.1016/j.epsl.2023.118384, 2023.

Liu, C., Lay, T., Wang, R. Taymaz, T., Xie, Z., Xiong, X., Irmak, T. S., Kahraman, M., and Erman, C.: Complex multi-fault rupture and triggering during the 2023 earthquake doublet in southeastern Türkiye, Nature Communication, 14, https://doi.org/10.1038/s41467-023-41404-5, 2023.

Lozos, J., Oglesby, D., Brune, J., and Olsen, K.: Small intermediate fault segments can either aid or hinder rupture propagation at stepovers, Geophysical Research Letters, 39, https://doi.org/10.1029/2012GL053005, 2012.

1119 Manighetti, I., Campillo, M., Bouley, S., and Cotton, F.: Earthquake scaling, fault
1120   segmentation, and structural maturity, Earth and Planetary Science Letters, 253,
1121   429-438, 2007.
1122 Manighetti, I., Mercier, A., and De Barros, L.: Fault trace corrugation and segmentation
1123   as a measure of fault structural maturity, Geophysical Research Letters, 48,
1124   https://doi.org/10.1029/2021GL095372, 2021.
1125 Mignan, A., Danciu, L., and Giardini, D.: Reassessment of the Maximum Fault Rupture
1126   Length of Strike-Slip Earthquakes and Inference on Mmax in the Anatolian
1127   Peninsula, Turkey, Seismological Research Letters, 86, 890-900, 2015.
1128 Nowicki, M., Wald, D., Hamburger, M., Hearne, M., and Thompson, E.:
1129   Development of a globally applicable model for near real-time
1130   prediction of
1131   seismically induced landslides, Engineering Geology, 173, 54-65, 2014.
1132 Pacheco, J., Scholz, C., and Sykes, L.: Changes in frequency-size relationship from
1133   small to large earthquakes, Nature, 355, 71-73, 1992.
1134 Pagani, M., Monelli, D., Weatherill, G., Danciu, L., Crowley, H., Silva, V., Henshaw,
1135   P., Butler, L., Nastasi, M., Panzeri, L., Simionato, M., and Vigano, D.: OpenQuake
1136   Engine: An Open Hazard (and Risk) Software for the Global Earthquake Model,
1137   Seismological Research Letters, 85, 692-702, 2014.
1138 Page, M., Field, E., Milner, K., and Powers, P.: The UCERF3 Grand Inversion: Solving
1139   for the Long-term rate of ruptures in a fault system, Bulletin of Seismological
1140   Society of America, 104, 1181-1204, 2014.
1141 Parker, R., Rosser, N., and Hales, T.: Spatial prediction of earthquake-
1142   induced landslide probability, Natural Hazards and Earth System Scien
1143   ces, Discussions, https://doi.org/10.5194/nhess-2017-193, 2017.
1144

Petersen, G. M., Büyükakpinar, P., Sanhueza, P. O. V., Metz, M., Cesca, S., Akbayram, K., Saul, J., and Dahm, T.: The 2023 Southeast Türkiye Seismic Sequence: Rupture of a Complex Fault Network, The Seismic Record, 3, 134-143, 2023.

Rangin, C., Maurin, T., and Masson, F.: Combined effects of Eurasia/Sunda oblique convergence and East-Tibetan crustal flow on the active tectonics of Burma, Journal of Asian Earth Sciences, 76, 185-194, 2013.

Rashidi, A., Shomali, Z. H., Dutykh, D., and Keshavarz Farajkhah, N.: Tsunami hazard assessment in the Makran subduction zone, Natural Hazards, 100, 2, 861-875, https://doi.org/10.1007/s11069-019-03848-1, 2020.

Ren, J., Zhang, S., Hou, Z., and Liu, X.: Study of Late Quaternary slip rate in the Mid-Segment of the Tongdian-Weishan fault, Seismology and Geology, 29, 756-764, 2007 (in Chinese with English abstract).

Rong, Y., Xu, X., Cheng, J., Chen, G., Magistrale, H., and Shen, Z.: A probabilistic seismic hazard model for mainland China, Earthquake Spectra, https://doi.org/10.1177/8755293020910754, 2020.

Schwartz, D., and K. Coppersmith.: Fault behavior and characteristic earthquakes: Examples from the Wasatch and San Andreas Fault Zones, Journal of Geophysical Research, 89, 5681-5698, 1984.

Shao, X., Ma, S., Xu, C., and Zhou, Q.: Effects of sampling intensity and non-slide/slide sample ratio on the occurrence probability of coseismic landslides, Geomorphology, 363, https://doi.org/10.1016/j.geomorph.2020.107222, 2020.

Shen, J., Wang, Y., and Ren, J.: Quaternary dextral strike slip motion of the Deqin-Daju-Daju fault zone, Yunnan, China, in: Study on the recent deformation and dynamic of the Lithosphere of Qinghai-Xizang Plateau, edited by: Ma, Z., Wang, Y., and

1170   Zhang, Y., Seismological Press, Beijing, China, 106-122, 2001 (in Chinese with

1171   English abstract).

1172 Shen, Z., Lu, J., Wang, M., and Burgmann, R.: Contemporary crustal deformation

1173   around the southeast borderland of the Tibetan Plateau, Journal of Geophysical

1174   Research, 110, https://doi.org/10.1029/2004JB003421, 2005.

1175 Shi, X., Sieh, K., Weldon, R., Zhu, C., Han, Y., Yang, J., and Robinson, S.: Slip rate and

1176   rare large prehistoric earthquakes of the Red River fault, southwestern China,

1177   Geochemistry,   Geophysics,   Geosystems,   19,

1178   https://doi.org/10.1029/2017GC007420, 2018.

1179 Stirling, M., Goded, T., Berryman, K., and Litchfield, N.: Selection of Earthquake

1180   Scaling Relationships for Seismic-Hazard Analysis, Bulletin of the Seismological

1181   Society of America, 103 (6), 2993-3011, 2013.

1182 Sun, C., Li, D., Shen, X., Kang, Y., Liu, R., and Zhang, Y.: Holocene activity evidence

1183   on the southeast boundary fault of Heqing basin, middle segment of Heqing-

1184   Eryuan fault zone, West Yunnan Province. China, Journal of Mountain Science,

1185   14, 1445-1453, 2017.

1186 Tang, Y., Hu, C., Tian, Q., Wang, L., Yang, P., and Xiong, R.: A Preliminary Study of

1187   Paleo-earthquakes in the Jianchuan Section of Longpan-Qiaohou Fault Zone,

1188   Yunnan Province, Earthquake, 34, 117-124, 2014 (in Chinese with English

1189   abstract).

1190 Tang, F., Ma, H., and Song, J.: Study on the Late Quaternary activity of Chenghai fault

1191   zone, Proceeding of the 16th World conference on earthquake engineering,

1192   Santiago, Chile, 1-9, 2017.

1193 Wang, E., Burchfiel, B. C., Royden, L. H., Chen, L., Chen, L., Li, W., and Chen, Z.:

1194   Late Cenozoic Xianshuihe-Xiaojiang, Red River, and Dali Fault Systems of

Southwestern Sichuan and Central Yunnan, China, Geological Society of America Special Paper, 327, 1-108, 1998.

Wang, Y., and Rathje, E.: Probabilistic seismic landslide hazard maps including epistemic uncertainty, Engineering Geology, 196, 313-324, 2015.

Wang, M., and Shen, Z.: Present‑Day Crustal Deformation of Continental China Derived from GPS and Its Tectonic Implications, Journal of Geophysical Research: Solid Earth, 125, https://doi.org/10.1029/2019JB018774, 2020.

Wells, D., and Coppersmith, K.: New empirical relationships among magnitude, rupture length, rupture width, rupture area, and surface displacement, Bulletin of Seismological Society of America, 84, 974-1002, 1994.

Wu, W., Long, F., Yang, J., Liang, M., Su, J., Wei, Y., Wu, P., and Lu, T.: Relocation, focal mechanisms and seismogenic structure of the 2013 Shangrila-Dêrong earthquake swarm sequence in the Yunnan-Sichuan border region, Chinese Journal of Geophysics, 58, 1584-1596, 2015 (in Chinese with English abstract).

Wu, F., Jiang, L., Zhang, G., and Song, Z.: The fault activity and seismic hazard assessment of central north segmentof the Deqin-Zhongdian fault, southeastern Qinghai-Tibet plateau, Acta Geologica Sinica, 93, 2657-2665, 2019 (in Chinese with English abstract).

Wu, X., Xu, X., Yu, G., Ren, J., Yang, X., Chen, G., Xu, C., Du, K., Huang, X., Yang, H., Li, K., and Hao, H.: China Active Faults Database and its web system, Earth System Science Data, https://doi.org/10.5194/essd-2023-119, 2023.

Xu, X., Wen, X., Zheng, R., Ma, W., Song, F., and Yu, G.: Pattern of latest tectonic motion and its dynamics for active blocks in Sichuan–Yunnan region, China, Science China Earth Sciences, 46, 210-226, 2003.

Xu, X., Wen, X., Yu, G., Chen, G., Klinger, Y., Hubbard, Y., and Shaw, J.: Coseismic reverse- and oblique-slip surface faulting generated by the 2008 Mw7.9 Wenchuan earthquake, China, Geology, 37, 515-518, 2009.

Xu, X., Wu, X., Yu, G., Tan, X., and Li, K.: Seismo-geological signatures for identifying $M \geq 7.0$ earthquake risk areas and their premilimary application in mainland China, Seismology and Geology, 39, 219-275, 2017 (in Chinese with English abstract).

Xu, W., Feng, G., Meng, L., Zhang, A., Ampuero, J., and Burgmann, R.: Transpressional rupture cascade of the 2016 Mw 7.8 Kaikoura earthquake, New Zealand, Journal of Geophysical Research: Solid Earth, 123, 2396-2409, 2018.

Xu, C., Xu, X., Zhou, B., and Shen, L.: Probability of coseismic landslides: A new generation of earthquake-triggered landslide hazard model, Journal of Engineering Geology, 27, 1122-1130, 2019 (in Chinese with English abstract).

Xu, L., Mohanna, S., Meng, L., Ji, C., Ampuero, J., Zhang, Y., Hasnain, M., Chu, R., and Liang, C.: The overall-subshear and multi-segment rupture of the 2023 Mw7.8 Kahramanmaras, Turkey earthquake in millennia supercycle. Communications Earth and Environment, 4, https://doi.org/10.1038/s43247-023-01030-x, 2023.

Yao, S., and Yang, H.: Towards ground motion prediction for potential large earthquakes from interseismic locking models, Earth and Planetary Science Letters, 601, https://doi.org/10.1016/j.epsl.2022.117905, 2023.

Youngs, R. and Coppersmith, K.: Implications of fault slip rates and earthquake recurrence models to Probabilistic Seismic Hazard estimates, Bulletin of Seismological Society of America, 75, 939-964, 1985.

Yu, W., Zhang, J., Zhou, G., Wang, J., and Zeng, X.: Surface Rupture of the 2001 Yongsheng *M*6 Earthquake and Chenghai Fault, Journal of Seismological Research, 28, 125-128, 2005 (in Chinese with English abstract).

Yu, Y., Li, S., and Xiao, L.: Development of ground motion attenuation relations for the new seismic hazard map of China, Technology for Earthquake Disaster Prevention, 8, 24-33, 2013 (in Chinese with English abstract).

Yu, L., Dong, Y., Zhou, W., Zhang, D., Wang, D., Yu, H., Ren, Y., and Li, J.: Evaluation of the rock uplift pattern in the Central Yunnan Subblock, SE Tibetan Plateau: Based on the Bedrock Channel Profile, Frontier in Earth Sciences, 10, https://doi.org/10.3389/feart.2022.821367, 2022.

Zhang, P., Shen, Z., Wang, M., Gan, W., Burgmann, R., Molnar, P., Wang, Q., Niu, Z., Sun, J., Wu, J., Sun, H., and You, X.: Continuous deformation of the Tibetan Plateau from global positioning system data, Geology, 32, 809-812, 2004.

Zhang, Z., Zhang, W., Chen, X., Li, P., and Fu, C.: Rupture dynamics and ground motion from potential earthquakes around Taiyuan, China, Bulletin of Seismological Society of America, 107: 1201-1212, 2017.

Zhang, Z., YAO, H., and Yang, Y.: Shear wave velocity structure of the crust and upper mantle in Southeastern Tibet and its geodynamic implications, Science China Earth Sciences, 63, 1278-1293, 2020.

Zhang, J., Chen, X., Cai, J., Liu, Z., Dong, Z., Guo, C., Han, B., Jiang, F., and Cui, T.: Magnetotelluric evidence for the crustal deformation beneath the region around the Lijiang-Xiaojinhe fault, SE margin of the Tibetan Plateau, Journal of Asian Earth Sciences, 235, https://doi.org/10.1016/j.jseaes.2022.105308, 2022.

Zhao, L., Xie, X., He, J., Tian, X., and Yao, Z.: Crustal flow pattern beneath the Tibetan Plateau constrained by regional Lg-wave Q tomography, Earth and Planetary

1270   Science Letters, 383, 113-122, 2013.

1271   Zhou, Q., Guo, S., and Xiang, H.: Principle and method of delineation of potential

1272   seismic sources in northeastern Yunnan Province, Seismology and Geology, 26,

1273   761-771, 2004 (in Chinese with English abstract).

1274   Zhou, R., Ye, Y., Li, Y., Li, X., He, Y., and Ge, T.: Late Quaternary activity of the

1275   Shawan segment of the Litang faults, Quaternary Sciences, 27, 45-53, 2007 (in

1276   Chinese with English abstract).

1277   Zhou, Y., Ren, C., Ghosh, A., Meng, H., Fang, L., Yue, H., Zhou, S., and Su, Y.:

1278   Seismological Characterization of the 2021 Yangbi Foreshock-Mainshock

1279   Sequence, Yunnan, China: More than a Triggered Cascade, Journal of Geophysical

1280   Research, 127, https://doi.org/10.1029/2022JB024534, 2022.